Journal Pre-proofs

Amphibole Control on Copper Systematics in Arcs: Insights from the Analysis of Global Datasets

Nicholas D. Barber, Marie Edmonds, Frances Jenner, Andreas Audétat, Helen Williams

Please cite this article as: Barber, N.D., Edmonds, M., Jenner, F., Audétat, A., Williams, H., Amphibole Control on Copper Systematics in Arcs: Insights from the Analysis of Global Datasets, *Geochimica et Cosmochimica Acta* (2021), doi: https://doi.org/10.1016/j.gca.2021.05.034

This is a PDF file of an article that has undergone enhancements after acceptance, such as the addition of a cover page and metadata, and formatting for readability, but it is not yet the definitive version of record. This version will undergo additional copyediting, typesetting and review before it is published in its final form, but we are providing this version to give early visibility of the article. Please note that, during the production process, errors may be discovered which could affect the content, and all legal disclaimers that apply to the journal pertain.
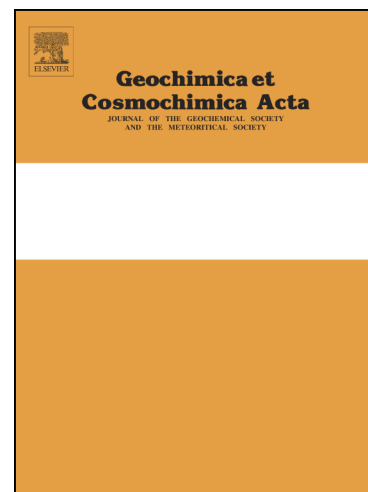
Amphibole Control on Copper Systematics in Arcs: Insights from the Analysis of Global Datasets

Nicholas D. Barber[1*], Marie Edmonds[1], Frances Jenner[2], Andreas Audétat[3], and Helen Williams[1]

[1]Department of Earth Sciences, University of Cambridge

[2]School of Environment, Earth, and Ecosystem Sciences, The Open University

[3]Bayerisches Geoinstitut, University of Bayreuth

April 28th, 2021

11 **Abstract**

12 Copper, sourced from porphyry deposits formed in arc settings, is a critical

13 resource, and is primarily sourced from magmas. However, the processes that

14 shape the copper contents of arc magmas are up for debate. Existing models

15 place emphasis on different petrological agents that explain large-scale trends

16 in copper systematics. Previous studies have noted the 'Cu paradox,' where

17 the magmas with high Sr/Y ratios, indicative of ore-forming potential, have the

18 lowest copper concentrations. Here we compile a multidimensional database of

19 volcanic whole rock compositions and couple it with simple petrological models

20 to elucidate the controls on volcanic whole rock compositions with respect to Cu.

21 We show that calc-alkaline, high Sr/Y magmas undergo major element modifica-

22 tion caused by extensive amphibole and/or garnet fractionation, which promotes

23 sulphide precipitation and copper depletion. We demonstrate the importance

24 of amphibole fractionation as a globally important process that promotes both

25 calc-alkaline differentiation and sulphide fractionation in arc magmas, as well

26 as its role in signalling the right set of chemical conditions in magmas that ul-

27 timately feed copper porphyry deposits. This work also raises the possibility of

28 amphibole as a geochemical and petrological indicator of potential porphyry-

29 forming conditions in a magma, which we show should be readily detectable by

30 a combination of different geochemical metrics. Despite their paucity in copper,

31 high Sr/Y magmas are associated with porphyry deposits, implying that the

32 propensity of magmas to form such deposits depends on factors other than a

33 magma's bulk copper content.

1   Introduction

Copper (Cu) is economically important owing to its role in the development of electrical components and its critical status in the transition to green energy[1]. Porphyry deposits, which are temporally and spatially associated with arc magmatism (Figure 1), account for over 70% of global Cu ore production[2], and significant amounts of Au and Mo[2]. Great progress has been made in developing a general model of porphyry development[3–9], yet more work needs to be done to understand how these processes are expressed in modern volcanic environments[10]. Prevailing magmatic models of Cu porphyry formation focus on two important processes, which may promote Cu enrichment, transport, and deposition in and around porphyry stocks: (i) the saturation of the magma in sulphide (an Fe and S-bearing liquid or mineral phase), into which Cu partitions strongly[11–17], a process which may deplete the magma Cu when sulphide fractionates, but may also enrich a magma if sulphide is remobilised by hotter or more oxidised magma[6,18–20]; and (ii) the exsolution of a volatile phase, which may unmix to a brine and vapor at low pressure[10], into which Cu and other metals partition and eventually precipitate from, leading to ore deposition[5,21–23].

A number of models have been proposed to explain how these processes may enhance a magma's potential to eventually go on and form a mineralized deposit. It has recently been suggested that sulphide saturation may be avoided by simultaneous Fe depletion and auto-oxidation caused by garnet fractionation[7]. Garnet's preference for Fe^{2+} leaves residual magmas enriched in Fe^{3+}[7]. This in turn produces a more oxidized and evolved melt (with higher S^{6+}/S^{2-}), which pushes the magma further away from sulphide saturation and may even trigger the dissolution of existing sulphides. It was proposed that this garnet-mediated process could enrich the melt in Cu, which could then be transferred to fluids when porphyry formation commences[7]. Alternatively, others have argued

1

61 that sulphide accumulation may be critical to later ore development by pre-

62 concentrating a reservoir of localized sulphides at the base of a magma reservoir[6],

63 where it is remobilised by intruding hotter or more oxidised magmas, thereby

64 enriching these magmas in Cu[6].

65 However, other studies have de-emphasized the importance of magmatic Cu

66 contents as an indicator of ore potential[3,24], promoting instead the importance

67 of magmatic water content[9,25,26], time scales of magma differentiation[27], and

68 larger magma volumes[28] as some of the critical controls on the capacity of a

69 magma to produce a porphyry. Nonetheless, nearly all models agree that the

70 process of sulphide saturation is important for understanding eventual ore for-

71 mation. Sulphide saturation is a complex process mediated by temperature,

72 pressure, and silicate melt composition, and thanks to continued empirical work

73 the factors leading to sulphide saturation in silicate melts are increasingly well

74 understood[29–34]. However, it is presently unclear (i) what petrological processes

75 in arc magmas will promote, delay, or are simply associated with sulphide frac-

76 tionation, and (ii) whether the early fractionation of a sulphide, and associated

77 loss of Cu, is detrimental to later porphyry formation[18].

78 One reason that these outstanding questions remain is the measure of sample

79 bias in our existing understanding of Cu systematics. Crucially, we need to es-

80 tablish what generic petrological processes, if any, can explain the abundances of

81 Cu in arc magmas in all major subduction zones. In order to address this need,

82 we compiled a large global database of volcanic arc whole rock compositions

83 (Figure 1). The ArcMetals database (N = 55,795) contains data from 17 arcs,

84 encompassing geochemical and contextual information such as major, trace el-

85 ement and radiogenic isotope compositions, geology, location, and geologic age

86 (see Methods), expanding on the approach taken by[3,7,20,26,35,36]. Combined,

87 these parameters allow us to explore Cu systematics in all arc settings. We

2

88 interpret the generic features of ArcMetals with respect to Cu systematics us-

89 ing models of silicate melt differentiation[37] and sulphide saturation[29] based on

90 recent high-quality experimental studies. This work pushes forward our under-

91 standing of key magmatic processes occurring in arcs that influence the capacity

92 of magmas to develop ore deposits. Furthermore, this work provides a frame-

93 work for further interrogation of major mineral controls on chalcophile metal

94 behaviour in specific volcanic arcs.

2 Methods

2.1 ArcMetals: Data Sources and Compilation

2.1.1 Database Design

98 This paper presents a new compilation of existing arc volcanic whole rock chem-

99 istry called *ArcMetals*. This database was compiled with several crucial design

100 distinctions in mind which distinguishes it from previous databases. First, we

101 wanted the database to be fully integrated with the spatial dimension of the

102 data. Hence, much of the compilation work takes place in a Geographic Infor-

103 mation System (GIS) environment, where we can control and append geophys-

104 ical and tectonic datasets. As discussed in greater detail both below and in the

105 Supplement, this approach afford us several advantages over prior compilations.

106 Here we take advantage of recent advances in the application of data science and

107 Geographic Information Systems (GIS) in geochemistry, allowing us to build on

108 prior studies that were based on simpler data compilation routines[3,7,20,25,35,36]

109 in the initial compilation and filtration of GeoRoc data, combining existing

110 petrological datasets in ore systematic ways. Subsequently, we apply a range of

111 geospatial techniques to append the maximum amount of geophysical data to

112 this compilation without compromising the extent or quality of this data. This

3

latter step is documented in detail in the Supplement, and is what sets this compilation apart from many previous datasets.

2.1.2 Geochemistry

Sample geochemical and analytical data were collected from the GeoRoc ([38]) database. These data were compiled using open source python code, available on GitHub (see link). Initially, 19 arc magma datasets were included in the database, but the Kermadec and Banda files contained so few data upon filtering, that they were ultimately omitted (Figure 1). Data for arc volcanic rocks were compiled (see Supplement). Before filtering, the fully compiled database contained > 200,000 records. In order to maximize the number of measurements per sample, six filters were applied to the initial compilation: (1) records with data obtained before 1960 C.E. were removed; (2) records with no recorded analytical technique were removed; (3) only those records pertaining to measurements by X-ray fluorescence (XRF), secondary ion mass spectrometry (SIMS), electron microprobe (EPMA), thermal ionization mass spectrometry (TIMS), inductively-coupled plasma mass spectrometry (ICP MS), laser ablation inductively-coupled plasma mass spectrometry (LA ICP MS), and Fourier transform infra red (FTIR) spectroscopy were retained; (4) the database was reduced to individual records where sample name, material type (whole rock, glass, or inclusion), and analytical technique were the same (e.g. if 1 whole rock sample had 4 records in GeoRoc measured using XRF, this filter would reduce the 4 records to one average for XRF); (5) records with the same sample name and material type were averaged and collapsed into one record. This had the effect of combining a sample's ICPMS measured trace elements with its XRF derived major elements; (6) samples that had the same element measured more than once using the same technique were removed. This filter only affected a small subset (a few hundred) samples, but having it in place makes it easier to

4

140 quantify analytical errors (see Supplement). Before plotting, the final database

141 was filtered to only include those magmas with a reported loss on ignition (LOI)

142 less than 3.5 wt.%, following standards in the literature[25]

2.1.3 Geophysical Parameters

144 Several global geophysical datasets were appended to the main database using

145 the geospatial software Quantum Geographic Information System, or QGIS 3.10.

146 The data appended included subducting slab surfaces and geometry generated

147 from extensive seismic records (slab dip, depth to slab, slab thickness)[39] , crustal

148 thickness ([40]), and subducting plate sediment cover thickness ([41]). Every sample

149 record in the database was linked to the geophysical datasets, which have good

150 global coverage at a resolution of 10-100 km^2. A sub-population of database

151 records had additional geophysical data appended based on their proximity to

152 volcanoes analyzed in Syracuse et al. 2006[42]. These data included convergence

153 rate, slab thermal parameter, and slab age[42]. The full QGIS methods and

154 compilation scripts can be found in the Supplementary Information Section.

3 Results

156 We present summaries of global volcanic whole rock geochemical data in Figures

157 2-5 and 9. These are discussed and interpreted in section 4, in light of modeling

158 done to validate these trends (Figure 6-8). Figure 2a shows volcanic whole rock

159 Sr/Y versus SiO_2, colour-coded for the different arcs (Figure 2b), Cu content

160 (Figure 2c) and crustal thickness (Figure 2d). It has been shown that magmas

161 fertile for porphyry Cu deposit formation have high whole rock Sr/Y ratios at

162 intermediate to felsic magma compositions (Figure 2,[25,35,43]). The Sr/Y ra-

163 tio, which compares the Large Ion Lithophile Element (LILE) Sr to the high

164 field strength element (HFSE) Y, is widely regarded as a proxy for high pres-

5

165 sure fractionation of hydrous arc magmas[20,25,43]. Strontium abundances during

166 fractionation are primarily controlled by plagioclase[44], whereas Y abundances

167 are controlled primarily by amphibole and garnet, as well as some minor phases

168 like titanite[45]. The ratio of plagioclase to amphibole crystallized in a fraction-

169 ating arc magma is decreased under conditions of high H_2O activity[46,47], which

170 simultaneously stabilizes amphibole phases which incorporate H_2O into their

171 structure[48]. Thus, a hydrous magma should see abundant amphibole fraction-

172 ation early in its differentiation in the mid to deep crust (up to 50 km.,[49–51])

173 and late-stage plagioclase crystallization at or near volatile saturation in the

174 upper crust[25]. This fractionation sequence will result in an elevated Sr/Y ratio

175 in deeply derived andesitic to dacitic magmas with significant amphibole[25].

176 Figure 3 shows MgO versus total FeO plots for global volcanic arc whole

177 rocks, colour-coded for Cu contents (Figure 3a and c), Sr/Y (Figure 3b) and

178 crustal thickness (CT; Figure 3d). These plots show that whole rocks with high

179 Cu contents lie along a tholeiitic trend (with Fe-enrichment), whereas those

180 whole rocks that lie along the calc-alkaline trajectory (with Fe depletion) are

181 copper-poor. These rocks also have the highest Sr/Y[25]. These observations are

182 consistent with previous work[3,7,20,52,53].

183 We identify the principal processes responsible for the geochemical trends

184 shown in Figures 2 and 3 using rare earth element (REE) concentrations (Figures

185 4 and 5). Figure 4 shows data sorted so that the highest [Cu] and Sr/Y points

186 are placed "on top" of the data cloud to ensure the reader is not missing any

187 of the highest [Cu] and Sr/Y points. However, there are many more low [Cu]

188 and Sr/Y points, as shown in the Supplement via 3D scatter plots set up using

189 the same axes and plot design (Figure S10). The schematics at the top of

190 both Figures 4 and 5 show vectors for the fractionation of garnet, amphibole,

191 olivine, plagioclase, orthopyroxene and clinopyroxene using an index of REE

6

192 plot curvature, Dy/Dy*[54]. Essentially, Dy/Dy* estimates the relative depletion

193 of the middle rare earth (MREE) Dy in relation to its light (LREE) and heavy

194 (HREE) counterparts. The Dy/Dy* metric makes a weighted determination of

195 the slope and shape of an REE spider diagram with respect to Dy, as:

$$\frac{Dy}{Dy*} = \frac{Dy_N}{La_N^{4/13} + Yb_N^{9/13}} \tag{1}$$

196 Dy/Dy* is of particular use for tracking amphibole/cpx and garnet fractionation[7,54–56]

197 in rock suites. Additionally, the trajectories for melting in the garnet source field

198 are plotted following[54]. The ratio Dy/Dy* tends to be lowered by amphibole

199 and clinopyroxene fractionation. These phases will deplete Dy relative to Yb.

200 Olivine, plagioclase, and orthopyroxene will drive Dy/Dy* towards higher val-

201 ues, as these phases do not incorporate Dy into their structure and thus Dy will

202 be enhanced relative to light (LREE) and heavy (HREE) rare earth elements.

203 Garnet fractionation will move Dy/Yb to higher values during fractionation

204 (i.e. deplete Yb relative to Dy) while simultaneously increasing Dy/Dy*. Man-

205 tle melting in the presence of garnet will lead to more moderate values of both

206 Dy/Yb and Dy/Dy* if a garnet rich source is extensively melted (see Discussion

207 section for more details).

208 The REE systematics of the global database can be further explored us-

209 ing a statistical approach[57], which compares parameters describing the shape

210 of chrondrite-normalized multi-REE plots (Figure 5). The REE polynomials,

211 symbolized by λ, describe the shape of REE curves[57] based on multivariate

212 statistics across all REE elements.[57] The polynomials are determined from the

213 following calculation in orthogonal form:

$$\ln([REE]/[REE]_{CI}) = \lambda_0 + \lambda_1 f_1^{orth} + \lambda_2 f_2^{orth} + \dots \tag{2}$$

7

Where the f variables represents polynomials of REE atomic radius (r_{REE}), chosen to avoid co-correlation of the λs[57]. A schematic at the side of Figure 5 shows the effect of fractionation of amphibole/cpx and garnet on REE systematics, expressed in terms of $\lambda 1$ and $\lambda 2$. Figure 5 is subsampled to only color magmas for Cu (Figure 5a) and Sr/Y (Figure 5b) where the whole rock composition shows Sr/Y > 50 (considered the "high Sr/Y" field in Figure 3). In the section below we discuss these geochemical data, present an interpretative framework, and place it within the context of previous studies.

4 Discussion

4.1 Geochemical Characteristics of High Sr/Y Magmas

We follow the lead of Loucks (2014), in recognizing the close association between high Sr/Y magmas and porphyry mineralization (Figure 2a[25]). Following this approach, this work shows that high Sr/Y magmas show an association with continental arcs such as Mexico, the Andes and the Cascades (Figure 2b and Supplementary Material), a low mean whole rock Cu concentration (< 50 ppm, (Figure 2c) and thicker crust (mean 40 km, Figure 2d) consistent with previous studies[3,20,35]. These same magmas also sit in the high Dy/Yb, low Dy/Dy* quadrant of Figure 4b, and the high $\lambda 2$, high $\lambda 1$ quadrant of Figure 5b. To confirm whether the mean Cu and crustal thickness differences in Figure 2 between high and low Sr/Y magmas is statistically robust, these values were compared using a two-way analysis of variance (ANOVA) hypothesis test, and subsequent Tukey's highly significant difference test. The null hypothesis tested in all cases was that the mean of a given measure is the same between two groups. The likelihood this is due to random chance is calculated using an F statistic, given by:

8

$$F = \frac{\Sigma n_j \left(\bar{X}_j - \bar{X}\right)^2 / (k-1)}{\sum \Sigma \left(X - \bar{X}_j\right)^2 / (N-k)} \tag{3}$$

239 Where n_j = the sample size in the jth group, $\bar{X}_j$ is the sample mean in
240 the jth group, $\bar{X}$ is the overall mean, k is the number of independent groups
241 in the analysis, and N is the total number of observations in the analysis[58].
242 This F-statistic is compared to a a critical-F at a given confidence threshold
243 and degrees of freedom. After determining the p-value, which is a simple but
244 easily misinterpreted measure of the likelihood of difference between the means
245 occurring due to random chance, the difference between the different treatments
246 (e.g. different arcs, different Sr/Y groups) is compared using a Tukey HSD test,
247 which calculates the following test statistic:

$$q_s = \frac{Y_A - Y_B}{SE} \tag{4}$$

248 where Y_A is the larger of the two means, Y_B the smaller, and SE the standard
249 error of the sum of the means. See the Supplement for detailed plots comparing
250 the test statistics, tables with statistical outputs and constraints, and the code
251 used in these analyses. The mean (1) Cu and (2) crustal thickness of the high
252 and low Sr/Y groups in Figures 2c and 2d have been compared, respectively,
253 using ANOVA tests, and these differences have been shown to be statistically
254 significant (p « 0.005) (see Supplementary Information for statistical tables).

255 The low mean Cu concentrations ([Cu]) in whole rocks associated with higher
256 Sr/Y (Figure 2c) highlights the so-called 'Cu-paradox'[7], where Cu is present
257 in low abundance in the magmas that appear to be most capable of forming
258 ore deposits. Observations such as these have been used to support porphyry
259 formation models where crystallization of sulphide removes Cu from the silicate
260 melts, to be later remobilized by one of several petrological processes[6,7,18,19].

9

261 However, it is also possible that melt [Cu] depletion may have little bearing on

262 whether a magma goes on to form an ore deposit[3,24]. While this initial analysis

263 confirms the findings of prior studies that magmatic [Cu] is significantly lower in

264 high Sr/Y magmas on a global scale[3,7,20], the petrological processes driving this

265 association have not yet been resolved. To address this, empiricla datasets are

266 combined with simple trace element partitioning and sulphide saturation models

267 are applied to better understand what petrological processes are associated with

268 high Sr/Y and low Cu in magmas.

4.2 Amphibole vs. Garnet Signatures

270 Globally, it can be seen that both low Cu (Figure 3a) and high Sr/Y (Figure

271 3b) volcanic whole rocks follow a calc-alkaline path, showing consistent Fe loss

272 with decreasing [MgO] (paralleling the high Sr/Y ellipse in Figure 3d). Similar

273 results were obtained by earlier data compilations[7,20,26,35]. Figure 3c and 3d

274 plot the binned FeO and MgO concentrations that have been smoothed to show

275 average FeO, MgO, Cu (Figure 3c), and crustal thickness (Figure 3d) at 0.05

276 wt.% MgO intervals. Figure 3c also shows the fractional crystallization paths

277 of experimentally synthesized and oxidized andesites and basalts[37], which also

278 lie on the calc-alkaline trend displayed by high Sr/Y magmas (more detail on

279 these in section 4.3).

280 Analysis of the global database suggests that high Sr/Y arc magmas share

281 key petrological features: they may undergo extensive fractionation of amphi-

282 bole +/- clinopyroxene and garnet (they extend into the bottom left quadrant

283 for Figure 4, upper right in Figure 5) and develop low Cu abundances during

284 progressive differentiation (Figure 4a, 5a). Whole rock compositions with the

285 highest Sr/Y ratios are characterized by concave-up REE profiles, where there is

286 both HREE depletion and overall enrichment in the LREE (Figure 4b). Figure

10

287 4b shows a strong preference for high Sr/Y magmas to sit in the bottom right

288 "garnet-influenced" quadrant (High Dy/Yb, low Dy/Dy*), and Figure 5a and

289 5b show many high Sr/Y whole rocks sitting near the amphibole fractionation

290 and garnet source field in $\lambda 1$ vs. $\lambda 2$ space (higher $\lambda 1$, higher $\lambda 2$). While there

291 is a clear association between high Sr/Y, low Cu magmas and the amphibole

292 fractionation field, the location of high Sr/Y magmas at low Dy/Dy* and mod-

293 erate Dy/Yb can also be explained through a magma formed in the "melting of

294 mantle garnet" field (bottom right quadrant) which subsequently experienced

295 (1) garnet fractionation at pressures around 1.2 GPa[51], followed by (2) amphi-

296 bole +/- clinopyroxene fractionation at lower pressures[51]. Whatever the exact

297 sequence of processes, a magma plotting in the bottom-right quadrant of Figure

298 4 must have experienced some HREE depletion and/or LREE enrichment to

299 match the predicted patterns of this metric[54]. Additionally, all magmas have

300 a starting REE profile that may not begin at the "crosshair" intersection of

301 the two bold black lines (defined for chrondritic-derived melt[54]). Rather, each

302 magma is likely derived from a mantle source with a unique REE profile de-

303 fined by prior melt extraction, metasomatism, and other pre- and syn-melting

304 features. Correcting for such source features is beyond the scope of this work,

305 but would be an interesting area of the global database to explore more fully.

306 The complexities of the petrogenesis leading to changes in Dy/Dy* should make

307 us cautious about using the Dy/Dy* systematics alone to diagnose the petro-

308 genesis of high Sr/Y magmas. Rather, any petrogenetic process proposed here

309 must be validated by other independent metrics, empirical observations, and/or

310 modeling.

311 This garnet to amphibole/cpx sequence may only be piecemeal at shallower

312 pressures, where amphibole/cpx will dominate as a fractionating phase out-

313 side the stability field for garnet[51]. Thus, while the importance of amphibole

11

314 in these systems will be demonstrated further, garnet likely also plays an im-
315 portant role, especially in the deep roots of arc magmatic systems[7,51,59]. By
316 the same logic, the influence of clinopyroxene cannot be ruled out, as cpx will
317 produce a similar compound fractionation trend as suggested by the blue line
318 for amphibole-garnet in Figure 4a, albeit with a steeper slope. Clinopyroxene
319 is one of the most common minerals in arc volcanic rocks, and empirical de-
320 terminations of pyroxene stability indicate that amphibole-friendly magmatic
321 conditions are comparably favourable for clinopyroxene[37,51]. However, amphi-
322 bole is favoured over clinopyroxene at higher magmatic water contents[51] and
323 lower temperatures[37,51] i.e. conditions more common in andesites stored in the
324 shallow to mid-crust (aligning with the conditions of magmatic storage prior
325 to porphyry formation[4]). Furthermore, the λ plots show less ambiguously that
326 high Sr/Y, low Cu magmas often have a much steeper slope, consistent with
327 amphibole control as opposed to cpx (Figure 5a, 5b). This emphasizes the im-
328 portance of combining geochemical metrics to get the most out of whole rock
329 data.

330 Garnet fractionation has gained popularity in the recent literature as a po-
331 tential ore fertility mechanism[7,55,59]. Experiments have shown that garnet is
332 stabilized as a fractionating phase at pressures above 0.8 GPa (approximately
333 24 km. depth)[51,60] and where melt water contents are high (above 4 wt. %)[51].
334 Direct evidence of garnet in arc magmas is rarely found in modern volcanics,
335 but it has been found commonly in fossil arc systems[61]. Whether ancient or
336 modern, where garnet can be seen widely in arc systems is in the lower crust
337 cumulate lithologies of exhumed "arc roots," sections like the type section in
338 Kohistan, Pakistan[62-64]. Models developed for the mantle wedge underlying
339 Central America found evidence for the presence of mantle heterogeneities rich
340 in garnet-peridotite or garnet pyroxenite lithologies[65]. Melting of such mantle

341 garnet "veins" would impart a signature with higher Dy/Yb than the arc array,

342 as discussed in detail in previous work[54,65].

343   While the role and importance of garnet fractionation is not disputed in ex-

344 plaining the occurrence of some magmas with low [Cu] in thicker-crust arcs[7,59],

345 this analysis suggests that amphibole is also an important candidate for moder-

346 ating global arc Cu systematics as shown in Figures 4 and 5. The importance of

347 amphibole has been previously proposed in the context of porphyry deposits[25]

348 and the broader controls on magmatic Fe[3], although in both of those cases REEs

349 were not used as a metric to measure amphibole's presence. Amphibole fraction-

350 ates in many arc magmatic environments at moderate (15-40 km.) depths[49,51],

351 while also being verifiable petrographically in volcanic products, either as a pri-

352 mary phase or as an exhumed xenolith[66]. Like garnet, amphibole is much more

353 stable at high melt H_2O contents[37,51,60], but unlike garnet it predominates at

354 moderate, not only deep crustal depths (20-55 km[49–51]) rather than just deep

355 depths. For many of the reasons the garnet hypothesis is favored, amphibole

356 can be similarly supported as an important chemical control on the bulk chem-

357 istry of arc magmas. Amphibole will be stabilised at moderate to temperatures

358 (between 800 and 1050 °C[37,51]), moderate to high pressure (0.7 - 1 GPa[49,51]),

359 and high water contents[51]. These results show, consistent with the literature,

360 the strong and unambiguous importance of the association between amphibole

361 in the fractionating assemblage and high Sr/Y magmas[3,9,20,25]. However, the

362 mechanism by which amphibole obtains such an association, particularly with

363 regards to [Cu], has not been explored in great detail in previous studies.

4.3 Amphibole Control on Melt Chemistry and Sulphide Stability

To understand how amphibole is able to affect these global Cu trends, it is necessary to show how amphibole can provide a link between high Sr/Y, calc-alkaline, potentially porphyry-developing magmas, and their low Cu contents. This is first done by analyzing the empirical results of a well-constrained series of isobaric fractional crystallization experiments[37] in the context of the low Cu, high Sr/Y magmas centered in this work (section 4.3.1). These empirical datasets are integrated with a trace element partitioning (reconstructing Cu, Ni, Sr, Y, and REE systematic) (4.3.1) and sulphide saturation (4.3.2) model to estimate the impact of amphibole on melt chemistry and subsequent sulphide systematics. Special attention is paid to amphibole's method of changing melt chemistry, with regards to the calc-alkaline differentiation trend discussed in Figure 3. All of these empirical and modeled observations are synthesized together by a simple mass balance model to link the fractionation of amphibole in andesites with the stabilization of sulphide and subsequent depletion of [Cu].

4.3.1 Analysis of Empirical Datasets

Trace element abundances of experimental results from an existing empirical study[37] were modeled to constrain the effect of amphibole on the liquid line of descent in arc magmas, in order to understand how amphibole fractionation may connect major and trace element systematics under high Sr/Y-favoring conditions. The experimental study in question ran isobaric experiments under equilibrium (EC) and fractional crystallization (FC) conditions at 1.0 GPa and from 1200 to 720 °C on hydrous oxidized basaltic[67] (called "FC Mb AuPd" in the original work) and oxidized andesitic (called "FC ba AuPd" in the original work) melts[68].

14

390   The experimental data used in this works' model[37] were prepared by tran-

391   scribing Table 1 (starting conditions), Table 2 (modal abundances of minerals

392   at each experimental temperature step), and Table 3 (glass and amphibole com-

393   positions, determined by EPMA) into Supplemental Data Table 4 of this work.

394   In Ulmer et al. 2018, major elements were the only measured chemical species.

395   Starting abundances of Ni, Cu, Sr, Y, and all REEs were taken from the trace el-

396   ement compositions of the relevant starting materials[46,67,68], and used to model

397   the partitioning of trace elements into fractionating mineral phases following

398   the methods of Shaw 2006[69]:

$$\frac{c_l^t}{c_o} = F^{D-1} \tag{5}$$

399   where t = timestep *t* in a given experiment, corresponding to a specific

400   set of T, P, and X_i conditions. Also called *run number* in 'ud' database; $c_l^t =$

401   concentration of an element in the residual liquid; c_o = initial concentration of

402   an element in bulk liquid, before fractionation; F^t = fraction of residual liquid

403    $\frac{L}{L_o}$; D^t = "Bulk D," or weighted sum of whole rock partition coefficients:

$$D^t = \sum_{i=0}^{\infty} X_i^t * D_{i-l}^t \tag{6}$$

404   where X_i = mass fraction of mineral *i* in accumulated solid fraction, and

405   D^{i-l} = partition coefficient (or K_d) between mineral *i* and liquid *l*. Final

406   form of Eqn. 5 requires that c_l is solved at each experimental step in the

407   differentiation sequences:

$$c_l = c_o * F^{D-1} \tag{7}$$

408   The effect of these trace element models on elements like Cu and Ni can be

409   found in the Supplement (Figure S11). Note that of the three FC experiments

15

410 total in the experimental database, only two are focused on in this work (the

411 oxidized runs). The results from Ulmer et al. 2018 experienced some empirical

412 complications around 900 °C, and the remaining melt fraction (F) and resul-

413 tant melt chemistry was reversed from what one would expect to occur naturally

414 (decreasing F with decreasing T). In order to make modeling these results as

415 straightforward as possible, runs 10-12 and 9-11 were discarded from the oxi-

416 dized andesite and oxidized basalt experimental runs respectively. One of the

417 most remarkable features of these empirical results is the well constrained liquid

418 line of descent (LLD) for calc-alkaline, hydrous, moderately oxidized magmas,

419 and the resulting association between LLD and major mineral phases like am-

420 phibole. Also remarkable is this empirical datasets constraint of the changes of

421 fO_2 with magmatic differentiation[37].

4.3.2   Comments on Amphibole's Effect on Mg#

423 Experimental work[37,49,51,70] has already implicated amphibole as one of the

424 most important phases controlling major element characteristics in high pres-

425 sure calc-alkaline magmas. However, invoking amphibole as an important agent

426 of melt chemistry change, as suggested f rom Figures 4 and 5, raises the ques-

427 tion of how amphibole, with an Fe/Mg exchange coefficient ratio of around

428 $\tilde{0}.3^{70}$, can maintain the consistent melt Mg# trend observed in calc-alkaline

429 suites (see Figure 3, high Sr/Y trend). The calc-alkaline trend observed in high

430 Sr/Y magmas sees a constant decrease of FeO with MgO, meaning that equal

431 proportions of both elements have to be leaving the melt to explain the changes

432 in melt chemistry. Despite the higher exchange coefficient of Mg in amphibole

433 as compared to Fe[49], some empirical work has noted that the majority of ma-

434 jor element differentiation in metaluminous/peraluminous magmas should be

435 controlled by amphibole at the relevant pressure and temperature conditions[51].

436   To test this, the relationship between amphibole, melt Mg#, and FeO con-

16

437 tents from the oxidized FC experiments[37] has been plotted in Figure 6. Where

438 amphibole stabilizes at 1050°C (Figure 6a), the Mg# of the melt does not see

439 the predicated rapid Mg# drop off as a function of either temperature (Figure

440 6a) or melt FeO wt.% (Figure 6b and c). Instead, melt Mg# decreases smoothly

441 through the amphibole stability field. Two major factors help to explain this

442 trend: (1) coexisting phases crystallizing at the same time as amphibole, and

443 (2) amphibole's increasing FeO content and correspondingly lower Mg# as the

444 magmas cools. Starting with the former, phases including clinopyroxene, gar-

445 net, plagioclase, ilmenite, and magnetite (in order of appearance) contribute

446 to changes in melt chemistry in the andesite, and in the basalt, this series of

447 other minerals also includes spinel. By mineral chemistry, phases like ilmenite,

448 magnetite, spinel, garnet (Fe/Mg exchange coefficient of around 0.7[51]), and even

449 clinopyroxene contain enough iron to explain the consistent decrease in FeO seen

450 in the empirical data modeled here. It should be noted however that amphibole

451 is one of the dominant minerals in the fractionating sequence following its initial

452 stabilization at 1050°C - thus, a good portion of the changes in melt chemistry

453 must be attributed to amphibole. Amphiboles stability may in fact be a marker

454 all on its own of the right conditions contributing to calc-alkaline differentia-

455 tion; contrast the trends seen in Figure 3 for the oxidized andesite and oxidized

456 basalt (Figure 3c) with that of the reduced basalt (FC ba Pt-C), where the lack

457 of amphibole contributes to the more tholeittic pattern of differentiation and a

458 lack of FeO depletion.

459 Furthermore as the empirical[37] melts' reach temperatures below 900°C, Fig-

460 ure 6b and 6c show that amphibole itself begins to take on more iron into its

461 structure. The stable amphibole species steps down from paragasite at temper-

462 atures > 900°C, to tschermakite (900°C), tschmerkatic hornblende (800 °C),

463 and finally magnesio-hornblende (720°C) at the end of each fractional crystal-

17

464 lization experiment (amphibole names follow established nomenclature[71]). Not

465 only does the FeO w.t% of amphibole increase with greater degrees of differen-

466 tiation, but Figure 6c sees a decrease in the Mg# of fractionating amphibole's

467 as well. Figure 6 shows that, consistent with the literature[37,49,51,70], amphibole

468 is not only associated with fractionating assemblages moving an arc magma to-

469 wards calc-alkaline differentiation, but it can indeed alter the FeO content of a

470 melt, in spite of its general preference for Mg cations over Fe. This extended

471 discussion of amphibole's impact on Fe is pertinent to the crucial element of

472 modeling done in this study, namely Fe's impact on sulphide saturation.

473 4.3.3 Integrating Sulphide Models into Empirical Results

474 To see whether major and trace element changes in a silicate melt affect the

475 stability of sulphides in the melt requires an empirical model of sulphide satura-

476 tion. Sulphide saturation is described by the experimental parameter, "sulphur

477 content at sulphide saturation," or SCSS[72]. Generally, SCSS is negatively cor-

478 related with pressure[72] and positively correlated with temperature[30,34,72], melt

479 H_2O content[73], melt FeO, Cu and Ni contents[12,30,72][12,29,30], and oxygen fugacity

480 (fO_2)[31,34,74]. For mid-ocean ridge basalts, melt FeO content, oxygen fugacity

481 (fO_2), temperature, and pressure are the main drivers of sulphide saturation[12].

482 In arc magmas, higher water and sulfur contents[21,75] coupled with higher oxi-

483 dation state[3,31] cause the SCSS to respond differently as compared to MORB,

484 though major elements like FeO still play a major role. For most arc mag-

485 mas, volatile and oxidation conditions lie outside the range for which many

486 SCSS models are calibrated[72], with some exceptions[31,73]. Since most arc mag-

487 mas have a considerable fraction of sulphur present as S^{6+}, they may instead

488 saturate in anhydrite, which is much more soluble in silicate melts[33].

489 SCSS was modeled for the oxidized basalt and oxidized andesite runs (Figure

490 3, 5, 6-8), using the major elements[37] and modeled trace elements (Cu, Ni) of

18

491 the individual products as inputs using a new SCSS paramterization[29]:

$$\ln\left[S^{2-}\right]_{\mathrm{SCSS}} = \Delta G^{O}_{FeO-FeS}/\mathrm{RT} + \ln C_{S^{2-}} - \ln a^{silmelt}_{FeO} + \ln a^{Sulf}_{FeS} \qquad (8)$$

492 This SCSS method builds on the work of[30], and is very sensitive to the bulk
493 silicate melt composition, the sulphide composition, Fe-Ni-Cu partitioning into
494 that sulphide, and P and T at ranges appropriate for these models[29]. For all ex-
495 periments, SCSS decreases with FeO and decreasing temperature (Figure 7a and
496 7b respectively)[72]. The SCSS values are initially calculated assuming the redox
497 state of the magma will favor mainly S^{2-}[29]. To account for the likely abundance
498 of S^{6+} , SCSS was calculated for a range of S^{6+} speciation end members based
499 on the ΔNNO buffer values for $f\mathrm{O}_2$ measured in the modeled experiments.
500 These values, 0.5, 1.0, and 1.5 ΔNNO, correspond to ΔQFM values of 0.78,
501 1.28, and 1.78 respectively (ΔNNO to ΔQFM conversion accomplished using
502 the Excel tool "Calc-fO2-buffer' from http://www.kaylaiacovino.com/tools-for-
503 petrologists/, using data from previous work[76]). These $f\mathrm{O}_2$ values translate to
504 $\frac{S^{6+}}{S_T}$ values of 0.2, 0.75, and 0.95 following a simple correction scheme developed
505 for oxidized magmas[77]:

$$SCSS_{Tot} = \frac{SCSS^{2-}}{\left(1 - \frac{S^{6+}}{\Sigma S}\right)} \qquad (9)$$

506 This in turn is based on an earlier parameterization of S^{6+} as a function of
507 ΔQFM buffer[31]:

$$\frac{S^{6+}}{S_T} = \frac{1}{1 + 10^{(2.1 - 2\Delta FMQ)}} \qquad (10)$$

508 Figure 7 shows the results of modeling the different S^{6+} abundances in the

19

509 magmas by using different symbols denoting the different oxidation state of S in
510 each empirical dataset. The onset of amphibole crystallization is shown both as
511 function of FeO (Figure 7a) and temperature (Figure 7b). To aid the reader in
512 understanding what major minerals are fractionating during the experiments,
513 a schematic blue line has been added to Figure 7a showing the major controls
514 on SCSS changes at different stages in the model. Where amphibole was the
515 dominant fractionating phase in these experiments, there was only secondary in-
516 volvement of minerals like garnet, magnetite, ilmentie, clinpyroxene, plagioclase,
517 and spinel, though amphibole become less abundant as temperature continued
518 to decrease[37]. High-temperature (>1050 °C) FeO loss is attributed to clinopy-
519 roxene and to a lesser extent orthopyroxene and olivine (only in the basalt),
520 followed by a much more amphibole (as well as garnet) mediated lowering of
521 SCSS at temperatures below 1050°C. These two FeO loss trends, clinopyroxene
522 vs. amphibole mediated, are separated by a small but abrupt decrease in SCSS,
523 which is a function of temperature change as clinopyroxene abundance decreases
524 and amphibole starts to appear (the "drop-off" on the blue curve in Figure 7a).

525   The onset of amphibole fractionation is associated with a continued lower-
526 ing of the SCSS, but no clear dramatic decrease (Figure 7a, b). However, if we
527 consider conditions relevant to porphyry development, clinopyroxene in these ex-
528 periments only fractionates at temperatures greater than 1050 °C, which should
529 be less common in the sort of mid-crust, high water, low Cu and high Sr/Y mag-
530 mas presumed to be important for developing porphyry systems. The comtin-
531 ued drop in SCSS as a function of FeO (Figure 7a) can be attributed to other
532 phases stabilzing alongside amphibole, and the increasing FeO and decreasing
533 Mg# trends seen in amphiboles from Figure 6b and 6c. Since arc magmas
534 usually contain bulk sulphur contents between 1000 and 2000 ppm (red box in
535 Figures 7a and 7b)[75], these models confirm that most hydrous arc magmas are

20

536 at or near sulphide saturation[3,24] during most of their differentiation, and as a
537 result will become depleted in Cu as sulphides are removed; this hypothesis can
538 be verified by further modeling (see 4.3.4). Furthermore, these magmas demon-
539 strate that even with $\frac{S^{6+}}{S_T}$ values approaching 0.75 at ΔQFM values greater than
540 1.2 (diamond and circle curves for andesite and basalt, respectively), sulphide
541 fractionation can be pervasive.

542 The noticeable but not necessarily dramatic decrease in SCSS at amphibole-
543 in is mediated by several competing factors: (1) As should be obvious from
544 the SCSS paramaterization above, FeO is the crucial oxide driving much of the
545 change in melt SCSS[29]. Of particular importance is the activity of FeO in the
546 melt, a_{FeO}, which is affected by the activity coefficient of FeO γ_{FeO} according
547 to Eqn. 8 (Eqn. 46 in original source[29]). (2) Different cations have a competing
548 effect in this γ term. For example, MgO has a strong negative correlation
549 with γ_{FeO}. This means that higher MgO will lower the activity coefficient of
550 FeO, mitigating the drop in SCSS as would be expected from FeO loss alone.
551 Should olivine or another mafic phase precede amphibole fractionation as is
552 the case for the oxidized basalt, the comparatively lower MgO will lead to a
553 strong increase in γ_{FeO}, magnifying the SCSS decrease. (3) By the same logic,
554 the strong positive correlation between Na, K, and γ_{FeO}, implies that a loss
555 of alkali elements will enhance SCSS reduction during amphibole fractionation.
556 So the SCSS-buffering effect is mitigated in part by a strong decrease in the
557 alkali content of the model melt, promoting the continued SCSS decrease seen
558 in Figure 7. (4) The $\ln a_{FeS}^{Sulf}$ term, or the activity of the sulphide itself, has
559 a large impact on SCSS. Related work has shown that the interplay between
560 the Fe, Cu, and Ni abundances in sulphide is a strong control on the SCSS[30].
561 Hence, the models of Cu and Ni abundance in the trace element partitioning
562 models included a small weight fraction (0.001) of sulphide fractionating at each

21

563 step, assuming the sulphide in question is a sulphide melt (see next section for

564 details), and using partition coefficients for Cu and Ni between sulphide melt

565 and silicate melt from[78]. These Kd's are 1070 for Cu, and 490 for Ni, taken from

566 experimental run LY04[78]. The consistent decrease of Cu and Ni in the silicate

567 melt leads to a concurrent decrease in the sulphide Fe/(Fe+Cu+Ni) content in

568 the hypothetical sulphide, and a corresponding decrease in the SCSS. Finally,

569 (5) the continual decrease in temperature at constant pressure as performed

570 in these experiments strongly affects the SCSS in the preferred SCSS model[29].

571 This approach to modeling SCSS alongside calc-alkaline differentiated magmas

572 shows the potential for amphibole to contribute to the modification of wholesale

573 melt chemistry.

574 4.3.4 Mass Balance of Amphibole's Effect on S

575 Figure 7 shows the almost wholly linear decrease of modeled SCSS as the ox-

576 idized andesite and basalt runs progress. However, SCSS alone only tells half

577 the story - to explain how amphibole fits into the story of the low Cu, high Sr/Y

578 magmas concerned in this work, there needs to be a compelling link between

579 this decrease in SCSS and the melt's sulphur content [S]. One way to demon-

580 strate this is to take a similarly simple FC modeling approach as was done for

581 the trace elements during the crystallization of the oxidized andesite and basalt.

582 This is made possible if (1) there is a [S] imposed on each empirical melt, (2) the

583 SCSS can be related to the [S] in such a way as to estimate the mass of sulphide

584 fractionating at each step, and (3) the melt [S] can subsequently have been

585 shown to have been perturbed by the modeled decrease in SCSS as a function

586 of amphibole.

587 The results of these models are shown in Figure 8. Figure 8a shows the wt%

588 of amphibole crystallizing in each experimental step[37]. Amphibole stabilizes at

589 35% crystallization (or F = 0.65) in the oxidized andesite (FC ba AuPd), and

22

590 63.70 % crystallization (F = 0.363) for the oxidized basalt (FC Mb AuPd)[37]. S

591 contents in the melt were estimated based on inventories of [S] in the literature[75],

592 as the starting experimental materials did not have reported measurements of

593 volatile trace elements like sulphur[37,67,68]. The modeling done here assumed

594 an oxidized arc basalt to have a starting [S] of 2000 ppm, or 0.2 wt.%[75]. An-

595 desites should have already experienced some [S] loss, either as a consequence of

596 degassing or as Figure 7c shows as a result of basaltic differentiation and subse-

597 quent sulphide fractionation - thus, the oxidized andesite series was modeled as

598 having a starting melt [S] of 1000 ppm (corresponding roughly to the point the

599 empirical basalt reached andesite-like melt compositions). Next, a simple mass

600 balance was adapted from earlier work[32] on sulphide's effect on [Cu] in MORB

601 composition magmas:

$$X_{sulf} = \frac{S_o - (SCSS)(X_{melt})}{S_{sulf}} \tag{11}$$

602 where X_{sulf} = the mass fraction of sulphide produced at each experimental

603 step; S_o = the starting [S] in each step (initially 2000 and 1000 ppm respectively

604 for the basalt and andesite); $SCSS$ = the modeled SCSS value[29]; X_{melt} = the

605 remaining fraction of melt, or F and; S_{sulf} = the wt.% concentration of sulphur

606 in the fractionating sulphide phase.

607 The goal of using this equation is to estimate the abundance of sulphide

608 leaving the system once SCSS and [S] become equivalent, and by extension to

609 model the decrease in [S] as a product of calc-alkaline differentiation. While the

610 prior modeling in this work coupled with the original empirical results provide

611 most of these parameters, this equation requires a fit to a particular sulphide

612 composition, S_{sulf}. A suitable arc magma sulphide is required, one which was

613 in equilibrium with basaltic to andesitic composition magmas, and which can

614 also house significant amounts of Cu and Ni. The sulphide chosen was an

23

615 average sulphide melt modeled to be the parent of lower-temperature sulphides

616 at Merapi volcano, Java, Indonesia[22]. Sulphide melts were preferred here over

617 other sulphide phases like pyrrhotite or cubanite because they are often primary

618 to the original melt, and only decompose into other, crystalline sulphide phases

619 at lower temperatures[22]. The average sulphide melt from Merapi was estimated

620 as having 38.2 wt.% S, 52000 ppm Cu, and $\tilde{2}300$ ppm Ni[22]. Fitting this value

621 to Eqn. 11 allows us to construct a mass balance of sulphur in the empirical

622 silicate melts analyzed in this study. The model results are presented as an Excel

623 worksheet and corresponding Python code in the Supplement. As previously

624 discussed, the silicate melts used here[37] correspond well to magmas stored at

625 moderate depth under high H_2O, moderate to high pressure conditions. Thus,

626 these results should be generalizable to many other hydrous arc andesites and

627 basalts analyzed from ArcMetals and other compilations.

628 Figure 8b and 8c shows that amphibole crystallization corresponds to almost

629 all of the sulphide fractionation and subsequent [S] loss in andesites. Starting

630 from a basalt, amphibole stabilizes too late, such that amphibole plays only a

631 marginal role in adjusting melt chemistry and corresponding sulphur and sul-

632 phide changes. Thus, conditions that favor olivine and pyroxene stability are

633 conducive to widespread sulphide fractionation in the most primitive arc basalts,

634 supporting our contention that most arc magmas experience pervasive sulphide

635 saturation. However, this work has been much more concerned with the kind

636 of andesitic, high Sr/Y magmas that would predominate in the mid- to lower

637 crust in porphyry-friendly settings. In andesites, amphibole is the only major

638 phase crystallizing when sulphides stabilize (Figure 8c). These coinciding trends

639 are the combination of a lower S_o (due to earlier basaltic sulphide fractionation)

640 combined with the earlier stabilization of amphibole and subsequent amphibole-

641 mediation of melt chemistry changes. Thus it seems where an andesite begins

24

642 to fractionate, amphibole is the dominant mediator of sulphide fractionation.
643 This fits with general observations that those high Sr/Y, low Cu magmas (with
644 measurable Dy/Dy* and λ deviations consistent with amphibole) are likely in-
645 termediate composition trapped at depth. These results also suggest that it is
646 amphibole-mediated changes in andesite melt chemistry, in turn a function of
647 melt temperature, that lowers SCSS enough to cause sulphide precipitation as
648 the [S] in the melt increases slowly as a an incompatible element until reaching
649 the SCSS (Figure 8c). This again highlights the importance of amphibole as
650 both a mediator of melt chemistry changes during calc-alkaline differentiation,
651 and a signal of the optimal conditions for calc-alkaline and low Cu conditions in
652 a melt. However, as Figure 7 showed, amphibole isn't radically changing melt
653 chemistry all on its own. Rather, the conditions associated with amphibole
654 crystallization (P, T, HO, fO2, melt chemistry) are conducive to a noticeable if
655 modest decreases in SCSS, FeO (and other major elements), [S] and thus mass of
656 sulphide fractionated and concurrent decrease in melt [Cu], where some but not
657 all of these changes are directly the effect of amphibole. Equally important but
658 not considered in depth in this work is the role of S degassing; should a magma
659 degas significant volumes of sulphur, such that [S] in the melt falls well below
660 the 1000+ ppm threshold set in Figure 8, there is little chance sulphides will
661 stabilize, and every chance that remaining sulphides will resorb and breakdown.

662   The presence of sulphides in magmas has been reported by an increasing
663 number of studies, in areas as diverse as Western North America[55], Kīlauea[77],
664 Réunion island[79], Tolbachik volcano, Kamchatka[80–82], Merapi[22,83] and Ijen[84,85]
665 volcanoes, Indonesia, the Ecuadorian[86] and Chilean Andean[56,59] volcanic zones,
666 and even sulphide-rich hornblende cumulate xenoliths[24,87]. The models and
667 analyses presented here (Figures 6-8), alongside the earlier compilations of whole
668 rock major and trace element data (Figure 2 through 5), provide compelling

669 evidence that amphibole fractionation is a both a contributor to and signal of

670 the cal-alkaline differentiation, extensive sulphide fractionation, and subsequent

671 melt [Cu] depletion. Another Fe-rich mineral, magnetite, has been implicated

672 in taking up substantial quantities of Fe^{3+}, which has been shown to lead to

673 reduction of S from S^{6+} to S^{2-}. Since sulphide saturates at much lower [S]

674 as compared to sulphate[19], higher proportions of S^{2-} will promote sulphide

675 fractionation and metal loss. The crucial difference here is that amphibole's

676 ability to promote sulphide fractionation and Cu loss is due to its reduction of

677 total melt FeO and other oxides (like Na_2O and K_2O), and amphibole's broader

678 stability throughout the differentiation history of an andesite. Furthermore, if

679 enough amphibole (and co-stable phases like ilmenite) reduce FeO enough, it is

680 possible that magnetite fractionation could be more limited.

4.4 Prevalence of Crystalline Sulphide Fractionation in Arc Volcanic Rocks

683 Our analysis of the global database demonstrates that amphibole fractionation,

684 accepted as one of the drivers of high whole rock Sr/Y signals[9,25,35], can promote

685 sulphide fractionation via Fe-loss and consequent Cu depletion in a typical calc-

686 alkaline magma. The sulphide concerned is likely to at first be a sulphide melt[22],

687 followed by a crystalline sulphide (e.g. monosulphide solid solution; MSS),

688 which should predominate in the lower temperature conditions of an arc magmas

689 as compared to MORB[17,87–89]. While the modeling in this study has been

690 concerned with the primary sulphide melt, a further consideration that needs

691 to be explored is whether there is direct evidence linking MSS fractionation

692 with Cu depletion in arc magmatic sequences. Such a connection would not

693 only emphasize the pervasiveness of sulphide fractionation in arc magmas, but

694 would also further implicate minerals like amphibole, clinopyroxene, and garnet

26

695 as controls sulphide stability. This study attempts to provide such evidence by

696 analyzing those whole rock compositions in ArcMetals that can be shown to have

697 fractionated MSS sulphide. Figure 9 plots whole rock Cu/Ag vs. MgO , coloured

698 for both Gd/Yb (Figure 9a), Dy/Dy* (Figure 9b), and for crustal thickness

699 (CT) (Figure 9c). The motivation behind constructing such plots stems from

700 the fact that Cu fractionates more strongly into MSS than Ag[13,78] (whereas the

701 opposite is true in sulphide melts; sulphide melt fractionation should promote

702 higher Cu/Ag), and such a ratio gives us the benefit of sensitively detecting the

703 presence of a fractionating MSS at sulphide saturation[53]. A low Cu/Ag ratio,

704 below average mid-ocean ridge basalt (MORB)[53,90] and continental crust[91], is

705 consistent with crystalline sulphide fractionation and consequent Cu removal

706 from the silicate melt[53] at lower temperatures than were modeled in Figure 8.

707 Gd/Yb (Figure 9a) is a proxy for garnet involvement in petrogenesis because

708 Gd partitions less strongly into garnet than Yb[90], and has been used to infer the

709 prevalence of garnet fractionation in the Andes[59]. The highest Gd/Yb ratios

710 are associated with whole rocks with the lowest Cu/Ag for a given MgO content

711 (Figure 8a), suggesting a direct correlation between the proportion of garnet

712 fractionation and the proportion of crystalline sulfide fractionation. Owing to

713 the complexities in analysing whole rocks for Ag, Cu/Ag datasets are rare and

714 are currently biased towards the Andes data, though there are some measure-

715 ments in other transitional arcs (Figure 8 symbols). There is no clear link be-

716 tween Cu/Ag in the whole rock and crustal thickness plot, but the very thickest

717 crust (>40 km) is associated with evolved volcanic rocks, with a higher Gd/Yb

718 (indicating garnet involvement) and low Cu/Ag. Figure 8b shows that lower

719 Dy/Dy*, indicative of amphibole, is also associated with low Cu/Ag, evolved

720 magmas. Thus, both garnet and amphibole are implicated in the petrogenesis of

721 magmas that have experienced the most sulphide fractionation. One drawback

27

722 to using Cu/Ag as a proxy for sulphides in the global database is the dearth of
723 available Ag and other chalcophile data in the literature. Only in the past 5-10
724 years have Ag and other difficult to measure elements become easily measurable
725 using ICPMS[53,56,59,77,92]. As studies reporting suites of chalcophile elements in
726 magmatic systems grow, future iterations of this database may yet be able to
727 make broader, more detailed analysis of Cu/Ag in arc systems. Furthermore,
728 our earlier modeling (Figure 7 and 8) suggest that a proxy like Cu/Ag is not
729 necessary to confirm sulphide fractionation, as sulphide fractionation should be
730 a ubiquitous phenomenon in arc magmas, thanks to changes in SCSS medi-
731 ated by phases like amphibole. However, natural data, without the benefit of
732 the kind of thermodynamic knowledge available in empirical datasets, can still
733 benefit form chalcophile trace element ratios like Cu/Ag

734 It is worth noting that the Gd/Yb content of a magma could be affected by
735 both garnet fractionation, or melt-derivation from a garnet rich source rock. If
736 the latter, one would expect small fractional melts to have high Gd/Yb followed
737 by progressively lower Gd/Yb as more and more Gd poor minerals melted out.
738 To pick apart these competing REE trends (shown schematically in Dy/Dy*
739 space in Figure 4, and in λ space in Figure 5) is beyond the scope of this work.
740 Prior work on Cu/Ag establishes that particular volcanoes in the Andes likely
741 experienced garnet fractionation as opposed to a mantle garnet signature[59]. One
742 way to assess how widespread mantle-garnet melting is as reflected in whole-
743 rock geochemical records would be to compare a suite of garnet-fractionating
744 rocks to a suite of candidate garnet-melting rocks, like those analyzed for REEs
745 in Central America[65]. A few well constrained cogenetic suites of rocks, analyzed
746 for REEs and plotted as a liquid line of descent in Dy/Dy* and λ space would
747 show what the relevant differences, if any, there are between garnet fractionation
748 and garnet melting in complex natural magmas.

28

749 Our schematic model (Figure 10) emphasizes the primary importance of
750 amphibole fractionation and the related importance of garnet/clinopyroxene
751 fractionation[7]. This work emphasizes the importance of amphibole as a po-
752 tentially widespread petrological-control mechanism that explains many of the
753 generic features of high Sr/Y magmas. The global applicability of this amphibole-
754 centred model complements garnet fractionation models, which work best in
755 arcs with mature magmatic columns, deep brittle-ductile transitions (which pro-
756 mote longer residence times of magma in crust[7]), and thicker crusts[7,59]. This
757 amphibole model also complements the more immature arc focused magnetite
758 fractionation models, which work best in young island arcs and/or back-arc
759 basins[19,90]. Our amphibole-centered model should be viewed on a continuum
760 with these other petrological models, where water-rich, calc-alkaline trending
761 arc magmas stored in the mid to deep crust (15-50 km.) will fractionate amphi-
762 bole and stabilize sulphide in "semi-mature" arcs (called "immature continental
763 arcs" as proposed in Lee et al. 2020, Figure 8b[7]). The exact depth of stor-
764 age, temeprature, fO_2, and amphibole stability in these magmas will depend
765 on many geological, chemical, and physical factors, as elaborated on in relevant
766 experimental results[37,49,51,70]. While the specific depth at which amphibole-
767 mediated SCSS reduction will occur is variable, the important feature to note
768 about this model is that amphibole represents a bridge between the magnetite-
769 dominated and garnet-dominated petrological models proposed in recent years.
770 As these semi-mature arcs evolve, garnet will fill much the same role as amphi-
771 bole in controlling Fe and stabilizing sulphide. This allows for a certain degree
772 of temporal evolution in the primary petrological vector controlling bulk [Cu]
773 in arc magmas, where one would expect a young, thermally immature arc to
774 modulate its Cu via magnetite[19], evolving to amphibole at a moderate maturity
775 and thickness, culminating in garnet-dominated Cu control by the time the arc

776 reaches maturity[7].

777   One point of departure with the analysis in this study as compared to pre-
778 vious studies relates the importance and timing of sulphide saturation. Some
779 studies[7,18] have assumed that early sulphide saturation is detrimental to even-
780 tual porphyry copper deposit development, articulating the 'Cu paradox,' of
781 low magmatic [Cu] being associated with ore deposits[7]. Studies using platinum
782 group elements as proxies for sulphide saturation in arc systems make this as-
783 sumption more explicit, arguing that ore development requires late sulphide
784 saturation[18]. However, as suggested in recent work[24], porphyry systems that
785 have experienced both prolonged amphibole fractionation and early sulphide
786 crystallization (and subsequent Cu loss) seem perfectly capable of developing
787 porphyry deposits later in their lifetime[24]. The global analysis shown here ap-
788 pears to confirm that melt Cu concentration does not act as a primary control
789 on the potential of a magma to go on and make a porphyry deposit. Similarly,
790 this amphibole-mediated SCSS reduction model does not imply that amphi-
791 bole fractionation is a critical missing link leading to porphyry development.
792 Rather, widespread amphibole fractionation (as reflected by the petrography
793 and/or whole-rock chemistry of a magma) is a consequence of particular mag-
794 matic conditions (P, T, $f\mathrm{O}_2$) that might, under the right geological conditions,
795 signal the right environment to develop a porphyry. Thus, amphibole is seen as
796 a driver of melt chemistry and SCSS changes, but more an indicator of, rather
797 than a driver of, porphyry development. In agreement with the observation
798 that high Sr/Y magmas have lower Cu concentrations[3,7] (Figure 3c), this anal-
799 ysis finds that combined amphibole and/or garnet fractionation of whole rock
800 chemistry (Figure 4,5) can lead to early sulphide saturation (Figure 7,8). The
801 low magmatic Cu concentrations observed in the high Sr/Y magmas in this
802 database are fundamentally the consequence of the deep, hydrous evolution of

30

803 arc magmas magmas. This crustal processing can lead to higher magmatic H_2O,

804 promoting amphibole +/- garnet stabilization, and subsequently lower the SCSS

805 enough to precipitate sulphides and reduce magmatic [Cu]. While this implies

806 that amphibole-dominated fractionation is thus a consequence of, rather than

807 the cause of, magmas being able to form porphyry deposits, amphiboles abun-

808 dance in deep-crust magmas is readily detectable by whole rock geochemistry,

809 and could be used alongside other proxies to assess magmatic ore potential in

810 porphyry settings.

811 5   Conclusion

812 In this study we present a comprehensive geochemical and geophysical database

813 of volcanic whole rock samples across 17 arcs covering most of the Earth's active

814 subduction zones. This database, ArcMetals, is differentiated from previous ef-

815 forts by a rigorous filtration and data compilation strategy. Here, we present

816 the first order features of thisArcMetals alongside a simple trace element and

817 sulphide saturation model to identify the key petrological processes that control

818 [Cu] in arc magmas. More importantly, there is a strong association between

819 high Sr/Y, calc-alkaline differentiation, and amphibole +/- garnet fractionation

820 in conditions relevant to porphyry deposits. High Sr/Y magmas show depletion

821 of FeO during calc-alkaline differentiation and are associated with significantly

822 lower whole rock mean Cu concentrations and thicker continental crust. We

823 show that trends are driven by extensive amphibole fractionation at temper-

824 atures below 1050°C, which lowers melt FeO (and other major elements) and

825 hence SCSS, driving widespread andesitic sulphide saturation and the removal

826 of Cu into early forming sulphide melts. As has been shown in previous work,

827 we contend that garnet fractionation can also contribute to Fe depletion, and

828 subsequently increases the likelihood of sulphide saturation at greater depths

829 before amphibole fractionates[7,59]. However, this is not necessary on its own to
830 stabilize sulphide. Rather, as our models of S in an empirical arc basalt show,
831 even olivine and clinopyroxene can mediate a substantial drop in SCSS, lead-
832 ing to sulphide fractionation. On the whole, sulphide fractionation should be
833 regarded as a widespread phenomenon early on in the history of arc magmas,
834 where processes like magnetite, amphibole, and garnet fractionation contribute
835 to overall changes in melt SCSS and melt [S].

836   Amphibole, this study's preferred petrological vector, provides a generic ex-
837 planation for global Cu systematics in semi-mature arc environments, as many
838 calc-alkaline, oxidized arc magmas with (1) moderate to high water contents,
839 (2) stored in the mid to deep crust at (3) moderate temperatures (800-1050°C)
840 are easily able to stabilize and fractionate amphibole, evidenced by Dy/Dy^*
841 and λ metrics and empirical data. Importantly, this analysis indicates that am-
842 phibole fractionation is, irrespective of the presence of garnet on the liquidus,
843 capable of lowering SCSS and promoting early sulphide saturation, and is a
844 useful indicator of the kind of geological conditions that might lead to later
845 porphyry development. Furthermore, while magmatic Cu contents are found
846 to be reflective of the crucial petrological processes identified in this and other
847 studies, [Cu] is not found to be a primary driver or proxy for ore fertility on its
848 own. Likewise, amphibole fractionation is a consequence of the kinds of con-
849 ditions conducive to porphyry development, and amphibole could be used as a
850 petrological and geochemical indicator for potential porphyry-developing mag-
851 mas. While many arc magmas fractionate amphibole[49] and most (if not all) arc
852 magmas are rich in water and other volatiles, porphyry deposits remain rare.
853 This study demonstrates early sulphide saturation is not necessarily detrimental
854 to later porphyry formation from a typical calc-alkaline arc magmas, and that
855 minerals like amphibole don't make porphyries, but rather are associated with

porphyry-friendly physical and chemical conditions. Even more crucial to this process is the tectonic (e.g. compressional stresses), geodynamic, geological, and temporal conditions of the magma reservoir system itself[4,24,25,93], which along with the geochemical factors analyzed here, strongly influence whether or not a porphyry system will form. It is possible that porphyry mineralization requires long timescales for differentiation and fluid segregation[4,25] under conducive crustal configurations, which could promote further amphibole crystallization in a melt-rich mid-crustal hot zone[4]. Larger magma volumes may be optimal for achieving extreme volatile concentration[94] (e.g. minimum 1000 km^3 for Bingham Canyon and other large porphyry deposits[4,27]), which would also favor porphyry mineralization[4,24–26].

References

1. Arndt, N. T. *et al.* Future global mineral resources. *Geochemical Perspectives* **6,** 1–171 (2017).

2. Singer, D. A., Berger, V. I., Menzie, W. D. & Berger, B. R. Porphyry copper deposit density. *Economic Geology* **100,** 491–514 (2005).

3. Richards, J. P. The oxidation state, and sulfur and Cu contents of arc magmas: implications for metallogeny. *Lithos* **233,** 27–45 (2015).

4. Chiaradia, M. & Caricchi, L. Stochastic modelling of deep magmatic controls on porphyry copper deposit endowment. *Scientific reports* **7,** 1–11 (2017).

5. Blundy, J., Mavrogenes, J., Tattitch, B., Sparks, S. & Gilmer, A. Generation of porphyry copper deposits by gas–brine reaction in volcanic arcs. *Nature Geoscience* **8,** 235–240 (2015).

6. Wilkinson, J. J. Triggers for the formation of porphyry ore deposits in magmatic arcs. *Nature Geoscience* **6,** 917. http://dx.doi.org/10.1038/ngeo1940%20http://10.0.4.14/ngeo1940%20https://www.nature.com/articles/ngeo1940#supplementary-information (Oct. 2013).

7. Lee, C.-T. A. & Tang, M. How to make porphyry copper deposits. *Earth and Planetary Science Letters* **529,** 115868 (2020).

8. Richards, J. Tectono-magmatic precursors for porphyry Cu-(Mo-Au) deposit formation. *Economic Geology* **98,** 1515–1533 (2003).

9. Richards, J. P. Magmatic to hydrothermal metal fluxes in convergent and collided margins. *Ore Geology Reviews* **40,** 1–26 (2011).

10. Hedenquist, J. W. & Lowenstern, J. B. The role of magmas in the formation of hydrothermal ore deposits. *Nature* **370,** 519–527. ISSN: 0028-0836. http://www.nature.com/doifinder/10.1038/370519a0 (Aug. 1994).

11. Kiseeva, E. S. & Wood, B. J. A simple model for chalcophile element partitioning between sulphide and silicate liquids with geochemical applications. *Earth and Planetary Science Letters.* ISSN: 0012821X (2013).

12. Kiseeva, E. S., Fonseca, R. O. & Smythe, D. J. Chalcophile elements and sulfides in the upper mantle. *Elements* **13,** 111–116 (2017).

13. Patten, C., Barnes, S.-J., Mathez, E. A. & Jenner, F. E. Partition coefficients of chalcophile elements between sulfide and silicate melts and the early crystallization history of sulfide liquid: LA-ICP-MS analysis of MORB sulfide droplets. *Chemical Geology* **358,** 170–188 (2013).

14. Jugo, P., Candela, P. & Piccoli, P. Magmatic sulfides and Au: Cu ratios in porphyry deposits: an experimental study of copper and gold partitioning at 850 C, 100 MPa in a haplogranitic melt–pyrrhotite–intermediate

34

905 solid solution–gold metal assemblage, at gas saturation. *Lithos* **46,** 573–
906 589 (1999).

907 15. Simon, A. C., Pettke, T., Candela, P. A., Piccoli, P. M. & Heinrich, C. A.
908 Copper partitioning in a melt–vapor–brine–magnetite–pyrrhotite assem-
909 blage. *Geochimica et Cosmochimica Acta* **70,** 5583–5600 (2006).

910 16. Li, Y. & Audétat, A. Effects of temperature, silicate melt composition,
911 and oxygen fugacity on the partitioning of V, Mn, Co, Ni, Cu, Zn, As, Mo,
912 Ag, Sn, Sb, W, Au, Pb, and Bi between sulfide phases and silicate melt.
913 *Geochimica et Cosmochimica Acta.* ISSN: 00167037 (2015).

914 17. Li, Y. & Audétat, A. Gold solubility and partitioning between sulfide liq-
915 uid, monosulfide solid solution and hydrous mantle melts: Implications
916 for the formation of Au-rich magmas and crust–mantle differentiation.
917 *Geochimica et Cosmochimica Acta* **118,** 247–262 (2013).

918 18. Park, J.-W. *et al.* Chalcophile element fertility and the formation of por-
919 phyry Cu±Au deposits. *Mineralium Deposita* **54,** 657–670 (2019).

920 19. Jenner, F. E., ONeill, H. S. C., Arculus, R. J. & Mavrogenes, J. A. The
921 magnetite crisis in the evolution of arc-related magmas and the initial
922 concentration of Au, Ag and Cu. *Journal of Petrology.* ISSN: 00223530
923 (2010).

924 20. Chiaradia, M. Copper enrichment in arc magmas controlled by overriding
925 plate thickness. *Nature Geoscience* **7,** 43–46 (2014).

926 21. Edmonds, M. & Mather, T. A. Volcanic sulfides and outgassing. *Elements.*
927 ISSN: 18115217 (2017).

928 22. Nadeau, O., Williams-Jones, A. E. & Stix, J. Sulphide magma as a source
929 of metals in arc-related magmatic hydrothermal ore fluids. *Nature Geo-*
930 *science.* ISSN: 17520894 (2010).

35

931 23. Audetat, A., Pettke, T., Heinrich, C. A. & Bodnar, R. J. Special paper: the composition of magmatic-hydrothermal fluids in barren and mineralized intrusions. *Economic Geology* **103,** 877–908 (2008).

934 24. Du, J. & Audétat, A. Early sulfide saturation is not detrimental to porphyry Cu-Au formation. *Geology* **48,** 519–524 (2020).

936 25. Loucks, R. Distinctive composition of copper-ore-forming arcmagmas. *Australian Journal of Earth Sciences* **61,** 5–16 (2014).

938 26. Rezeau, H. & Jagoutz, O. The importance of H2O in arc magmas for the formation of porphyry Cu deposits. *Ore Geology Reviews,* 103744 (2020).

940 27. Chelle-Michou, C., Rottier, B., Caricchi, L. & Simpson, G. Tempo of magma degassing and the genesis of porphyry copper deposits. *Scientific reports* **7,** 40566 (2017).

943 28. Steinberger, I., Hinks, D., Driesner, T. & Heinrich, C. A. Source plutons driving porphyry copper ore formation: combining geomagnetic data, thermal constraints, and chemical mass balance to quantify the magma chamber beneath the Bingham Canyon deposit. *Economic Geology* **108,** 605–624 (2013).

948 29. O'Neill, H. The thermodynamic controls on sulfide saturation in silicate melts with application to Ocean Floor Basalts. (2020).

950 30. Smythe, D. J., Wood, B. J. & Kiseeva, E. S. The S content of silicate melts at sulfide saturation: new experiments and a model incorporating the effects of sulfide composition. *American Mineralogist* **102,** 795–803 (2017).

954 31. Jugo, P. J., Wilke, M. & Botcharnikov, R. E. Sulfur K-edge XANES analysis of natural and synthetic basaltic glasses: Implications for S speciation

956 and S content as function of oxygen fugacity. *Geochimica et Cosmochimica*

957 *Acta* **74,** 5926–5938 (2010).

958 32. Kiseeva, E. S. & Wood, B. J. The effects of composition and temperature

959 on chalcophile and lithophile element partitioning into magmatic sulphides.

960 *Earth and Planetary Science Letters* **424,** 280–294 (2015).

961 33. Zajacz, Z. & Tsay, A. An accurate model to predict sulfur concentration at

962 anhydrite saturation in silicate melts. *Geochimica et Cosmochimica Acta*

963 **261,** 288–304 (2019).

964 34. Nash, W. M., Smythe, D. J. & Wood, B. J. Compositional and tempera-

965 ture effects on sulfur speciation and solubility in silicate melts. *Earth and*

966 *Planetary Science Letters* **507,** 187–198. ISSN: 0012-821X. http://www.

967 sciencedirect.com/science/article/pii/S0012821X18307155 (2019).

968 35. Chiaradia, M. Crustal thickness control on Sr/Y signatures of recent arc

969 magmas: an Earth scale perspective. *Scientific reports* **5,** 8115 (2015).

970 36. Farner, M. J. & Lee, C.-T. A. Effects of crustal thickness on magmatic

971 differentiation in subduction zone volcanism: a global study. *Earth and*

972 *Planetary Science Letters* **470,** 96–107 (2017).

973 37. Ulmer, P., Kaegi, R. & Müntener, O. Experimentally derived intermediate

974 to silica-rich arc magmas by fractional and equilibrium crystallization at

975 1· 0 GPa: An evaluation of phase relationships, compositions, liquid lines

976 of descent and oxygen fugacity. *Journal of Petrology* **59,** 11–58 (2018).

977 38. Sarbas, B. & Nohl, U. The GEOROC database as part of a growing geoin-

978 formatics network. *Geoinformatics* (2008).

979 39. Hayes, G. P. *et al.* Slab2, a comprehensive subduction zone geometry

980 model. *Science* **362,** 58–61 (2018).

37

40. Szwillus, W., Afonso, J. C., Ebbing, J. & Mooney, W. D. Global crustal thickness and velocity structure from geostatistical analysis of seismic data. *Journal of Geophysical Research: Solid Earth* **124,** 1626–1652 (2019).

41. Pasyanos, M. E., Masters, T. G., Laske, G. & Ma, Z. LITHO1. 0: An updated crust and lithospheric model of the Earth. *Journal of Geophysical Research: Solid Earth* **119,** 2153–2173 (2014).

42. Syracuse, E. M. & Abers, G. A. Global compilation of variations in slab depth beneath arc volcanoes and implications. *Geochemistry, Geophysics, Geosystems.* ISSN: 15252027 (2006).

43. Richards, J. P. High Sr/Y ratio magmas and porphyry Cu, Mo, Au Deposits:Just add water. *Economic Geology* **106,** 1075–1081. ISSN: 0361-0128. http://dx.doi.org/10.2113/econgeo.106.7.1075 (Nov. 2011).

44. Ewart, A. & Griffin, W. Application of proton-microprobe data to trace-element partitioning in volcanic rocks. *Chemical Geology* **117,** 251–284 (1994).

45. Green, T. H. Experimental studies of trace-element partitioning applicable to igneous petrogenesis—Sedona 16 years later. *Chemical Geology* **117,** 1–36 (1994).

46. Grove, T., Parman, S., Bowring, S., Price, R. & Baker, M. The role of an H 2 O-rich fluid component in the generation of primitive basaltic andesites and andesites from the Mt. Shasta region, N California. *Contributions to Mineralogy and Petrology* **142,** 375–396 (2002).

47. Stolper, E. Water in silicate glasses: an infrared spectroscopic study. *Contributions to Mineralogy and Petrology* **81,** 1–17 (1982).

48. Foden, J. & Green, D. Possible role of amphibole in the origin of andesite: some experimental and natural evidence. *Contributions to Mineralogy and Petrology* **109,** 479–493 (1992).

49. Ridolfi, F., Renzulli, A. & Puerini, M. Stability and chemical equilibrium of amphibole in calc-alkaline magmas: an overview, new thermobarometric formulations and application to subduction-related volcanoes. *Contributions to Mineralogy and Petrology* **160,** 45–66 (2010).

50. Santana, L. V., McLeod, C., Blakemore, D., Shaulis, B. & Hill, T. Bolivian hornblendite cumulates: Insights into the depths of Central Andean arc magmatic systems. *Lithos,* 105618 (2020).

51. Alonso-Perez, R., Müntener, O. & Ulmer, P. Igneous garnet and amphibole fractionation in the roots of island arcs: experimental constraints on andesitic liquids. *Contributions to Mineralogy and Petrology* **157,** 541 (2009).

52. Lee, C.-T. A. *et al.* Copper systematics in arc magmas and implications for crust-mantle differentiation. *Science* **336,** 64–68 (2012).

53. Jenner, F. E. Cumulate causes for the low contents of sulfide-loving elements in the continental crust. *Nature Geoscience.* ISSN: 17520908 (2017).

54. Davidson, J., Turner, S. & Plank, T. Dy/Dy*: variations arising from mantle sources and petrogenetic processes. *Journal of Petrology* **54,** 525–537 (2013).

55. Chen, K. *et al.* Sulfide-bearing cumulates in deep continental arcs: The missing copper reservoir. *Earth and Planetary Science Letters,* 115971 (2019).

56. Cox, D., Watt, S. F., Jenner, F. E., Hastie, A. R. & Hammond, S. J. Chalcophile element processing beneath a continental arc stratovolcano. *Earth and Planetary Science Letters* **522,** 1–11 (2019).

39

1031 57. O'Neill, H. S. C. The smoothness and shapes of chondrite-normalized rare
1032 earth element patterns in basalts. *Journal of Petrology* **57,** 1463–1508
1033 (2016).

1034 58. Sullivan, L. *Hypothesis Testing - Analysis of Variance (ANOVA)* `https://`
1035 `sphweb.bumc.bu.edu/otlt/MPH-Modules/BS/BS704_HypothesisTesting-`
1036 `ANOVA/BS704_HypothesisTesting-Anova_print.html`.

1037 59. Cox, D. *et al.* Elevated magma fluxes deliver high-Cu magmas to the upper
1038 crust. *Geology* **48** (2020).

1039 60. Greene, A. R., DeBARI, S. M., Kelemen, P. B., Blusztajn, J. & Clift, P. D.
1040 A detailed geochemical study of island arc crust: the Talkeetna arc section,
1041 south–central Alaska. *Journal of Petrology* **47,** 1051–1093 (2006).

1042 61. Bissig, T., Leal-Meja, H., Stevens, R. B. & Hart, C. J. High Sr/Y magma
1043 petrogenesis and the link to porphyry mineralization as revealed by Garnet-
1044 Bearing I-type granodiorite porphyries of the Middle Cauca Au-Cu Belt,
1045 Colombia. *Economic Geology* **112,** 551–568 (2017).

1046 62. Petterson, M. The plutonic crust of Kohistan and volcanic crust of Kohistan–
1047 Ladakh, north Pakistan/India: lessons learned for deep and shallow arc
1048 processes. *Geological Society, London, Special Publications* **483,** 123–164
1049 (2019).

1050 63. Jan, M. Q. & Howie, R. The mineralogy and geochemistry of the meta-
1051 morphosed basic and ultrabasic rocks of the Jijal complex, Kohistan, NW
1052 Pakistan. *Journal of Petrology* **22,** 85–126 (1981).

1053 64. Ducea, M. N., Saleeby, J. B. & Berganz, G. The architecture, chemistry,
1054 and evolution of continental magmatic arcs. *Annual Review of Earth and*
1055 *Planetary Sciences* **43,** 299–331 (2015).

65. Feigenson, M. D. & Carr, M. J. The source of Central American lavas: inferences from geochemical inverse modeling. *Contributions to Mineralogy and Petrology* **113,** 226–235 (1993).

66. Jeffery, A. J. *et al.* The pre-eruptive magma plumbing system of the 2007–2008 dome-forming eruption of Kelut volcano, East Java, Indonesia. *Contributions to Mineralogy and Petrology* **166,** 275–308 (2013).

67. Hürlimann, N. *et al.* Primary magmas in continental arcs and their differentiated products: petrology of a post-plutonic dyke suite in the Tertiary Adamello batholith (Alps). *Journal of Petrology* **57,** 495–534 (2016).

68. Baker, M. B., Grove, T. L. & Price, R. Primitive basalts and andesites from the Mt. Shasta region, N. California: products of varying melt fraction and water content. *Contributions to Mineralogy and Petrology* **118,** 111–129 (1994).

69. Shaw, D. M. *et al. Trace elements in magmas: a theoretical treatment* (Cambridge University Press, 2006).

70. Nandedkar, R. H., Hürlimann, N., Ulmer, P. & Müntener, O. Amphibole–melt trace element partitioning of fractionating calc-alkaline magmas in the lower crust: an experimental study. *Contributions to Mineralogy and Petrology* **171,** 71 (2016).

71. Leake, B. E. *et al.* Nomenclature of amphiboles; report of the subcommittee on amphiboles of the International Mineralogical Association, Commission on New Minerals and Mineral Names. *The Canadian Mineralogist* **35,** 219–246 (1997).

72. O'Neill, H. & Mavrogenes, J. A. The sulfide capacity and the sulfur content at sulfide saturation of silicate melts at 1400 C and 1 bar. *Journal of Petrology* **43,** 1049–1087 (2002).

41

73. Fortin, M.-A., Riddle, J., Desjardins-Langlais, Y. & Baker, D. R. The effect of water on the sulfur concentration at sulfide saturation (SCSS) in natural melts. *Geochimica et Cosmochimica Acta* **160,** 100–116 (2015).

74. Jugo, P. J. Sulfur content at sulfide saturation in oxidized magmas. *Geology* **37,** 415–418 (2009).

75. Wallace, P. J. & Edmonds, M. The sulfur budget in magmas: evidence from melt inclusions, submarine glasses, and volcanic gas emissions. *Reviews in Mineralogy and Geochemistry* **73,** 215–246 (2011).

76. Frost, B. R. *et al.* A geochemical classification for granitic rocks. *Journal of petrology* **42,** 2033–2048 (2001).

77. Wieser, P., Jenner, F., Edmonds, M., Maclennan, J. & Kunz, B. Chalcophile elements track the fate of sulfur at Kilauea Volcano, Hawai'i (2020).

78. Li, Y. & Audetat, A. Partitioning of V,Mn, Co, Ni,Cu,Zn,As,Mo,Ag,Sn,Sb,W,Au,Pb, and Bi between sulphide phases and hydrous basanite melt at upper mantle conditions. *Earth and Planetary Science Letters* (2012).

79. Collins, S., Maclennan, J., Pyle, D., Barnes, S.-J. & Upton, B. Two phases of sulphide saturation in Réunion magmas: Evidence from cumulates. *Earth and Planetary Science Letters* **337,** 104–113 (2012).

80. Kamenetsky, V. S. *et al.* Silicate-sulfide liquid immiscibility in modern arc basalt (Tolbachik volcano, Kamchatka): Part II. Composition, liquidus assemblage and fractionation of the silicate melt. *Chemical Geology* **471,** 92–110 (2017).

81. Kamenetsky, V. S. & Zelenski, M. Origin of noble-metal nuggets in sulfide-saturated arc magmas: A case study of olivine-hosted sulfide melt inclusions from the Tolbachik volcano (Kamchatka, Russia). *Geology* **48,** 620–624 (2020).

82. Zelenski, M., Kamenetsky, V., Mavrogenes, J., Gurenko, A. & Danyu-shevsky, L. Silicate-sulfide liquid immiscibility in modern arc basalt (Tol-bachik volcano, Kamchatka): Part I. Occurrence and compositions of sul-fide melts. *Chemical Geology* **478,** 102–111 (2018).

83. Nadeau, O., Stix, J. & Williams-Jones, A. E. The behavior of Cu, Zn and Pb during magmatic–hydrothermal activity at Merapi volcano, Indonesia. *Chemical Geology* **342,** 167–179 (2013).

84. Berlo, K., van Hinsberg, V., Vigouroux, N., Gagnon, J. & Williams-Jones, A. Sulfide breakdown controls metal signature in volcanic gas at Kawah Ijen volcano, Indonesia. *Chemical Geology* **371,** 115–127 (2014).

85. Nadeau, O., Stix, J. & Williams-Jones, A. E. Links between arc volcanoes and porphyry-epithermal ore deposits. *Geology.* ISSN: 19432682 (2016).

86. Georgatou, A., Chiaradia, M., Rezeau, H. & Wälle, M. Magmatic sulphides in Quaternary Ecuadorian arc magmas. *Lithos* **296,** 580–599 (2018).

87. Chang, J. & Audétat, A. Petrogenesis and metal content of hornblende-rich xenoliths from two Laramide-age magma systems in southwestern USA: insights into the metal budget of arc magmas. *Journal of Petrology* **59,** 1869–1898 (2018).

88. Keith, M., Haase, K. M., Klemd, R., Schwarz-Schampera, U. & Franke, H. Systematic variations in magmatic sulphide chemistry from mid-ocean ridges, back-arc basins and island arcs. *Chemical Geology.* ISSN: 00092541 (2017).

89. Rottier, B., Audétat, A., Koděra, P. & Lexa, J. Origin and Evolution of Magmas in the Porphyry Au-mineralized Javorie Volcano (Central Slo-vakia): Evidence from Thermobarometry, Melt Inclusions and Sulfide In-clusions. *Journal of Petrology* **60,** 2449–2482 (2019).

43

90. Jenner, F. E. *et al.* Chalcophile element systematics in volcanic glasses from the northwestern Lau Basin. *Geochemistry, Geophysics, Geosystems.* ISSN: 15252027 (2012).

91. Holland, H. D. & Turekian, K. K. Treatise on geochemistry (2004).

92. Jenner, F. E. & Arevalo, R. D. Major and trace elerment analysis of natural and experimental igneous systems using LA-ICP-MS. *Elements.* ISSN: 18115217 (2016).

93. Richards, J. P. A Shake-Up in the Porphyry World? *Economic Geology* **113,** 1225–1233. ISSN: 0361-0128. http://dx.doi.org/10.5382/econgeo.2018.4589 (Sept. 2018).

94. Rohrlach, B. D., Loucks, R. R. & Porter, T. Multi-million-year cyclic ramp-up of volatiles in a lower crustal magma reservoir trapped below the Tampakan copper-gold deposit by Mio-Pliocene crustal compression in the southern Philippines. *Super porphyry copper and gold deposits: A global perspective* **2,** 369–407 (2005).

Data Availability

All of our data, code, and protocols are available at the corresponding author's GitHub: https://github.com/ndb38/slab_metals. This current link is subject to change: the database and all associated code is going to be stream lined into a less crowded repository in future versions, and allowed to virtually run through Binder. The code and figures will be updated in future versions of the database, but all the material pertaining to this paper will be preserved.

44

Acknowledgements

Author Contributions

NDB conceived the project with advice and comments from ME and FJ. NDB compiled the database, wrote the Python code, and performed the analysis. ME., FJ, AA, and HW provided equal contributions regarding data interpretations and significant references. NDB wrote the manuscript with equal editing contributions from ME, FJ, AA, and HW.

Competing Interests

The authors declare no competing interests.

45

1177 Materials and Correspondence

1178 All correspondence should be directed to Nicholas Barber (ndb38@cam.ac.uk).

1179 Figures
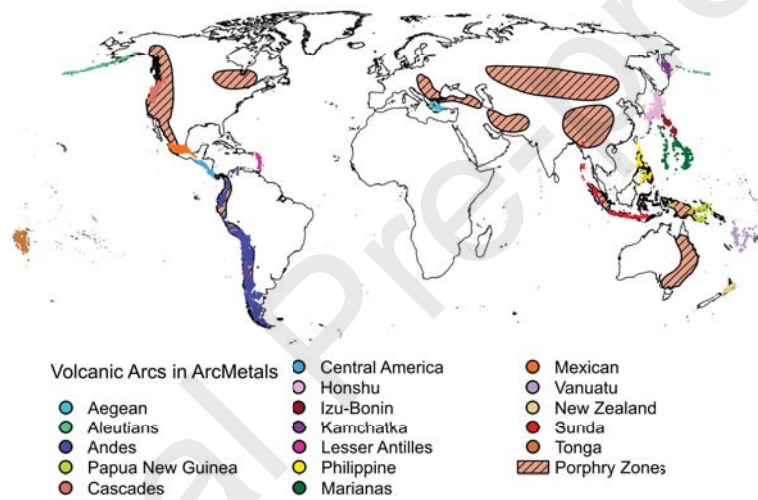
Figure 1: Global distribution of samples used in ArcMelts2, our global data compilation. Sample locations are color coded by arc. Samples are overlayed on zones of porphyry mineralization, taken from [2]. Created using QGIS 3.10.
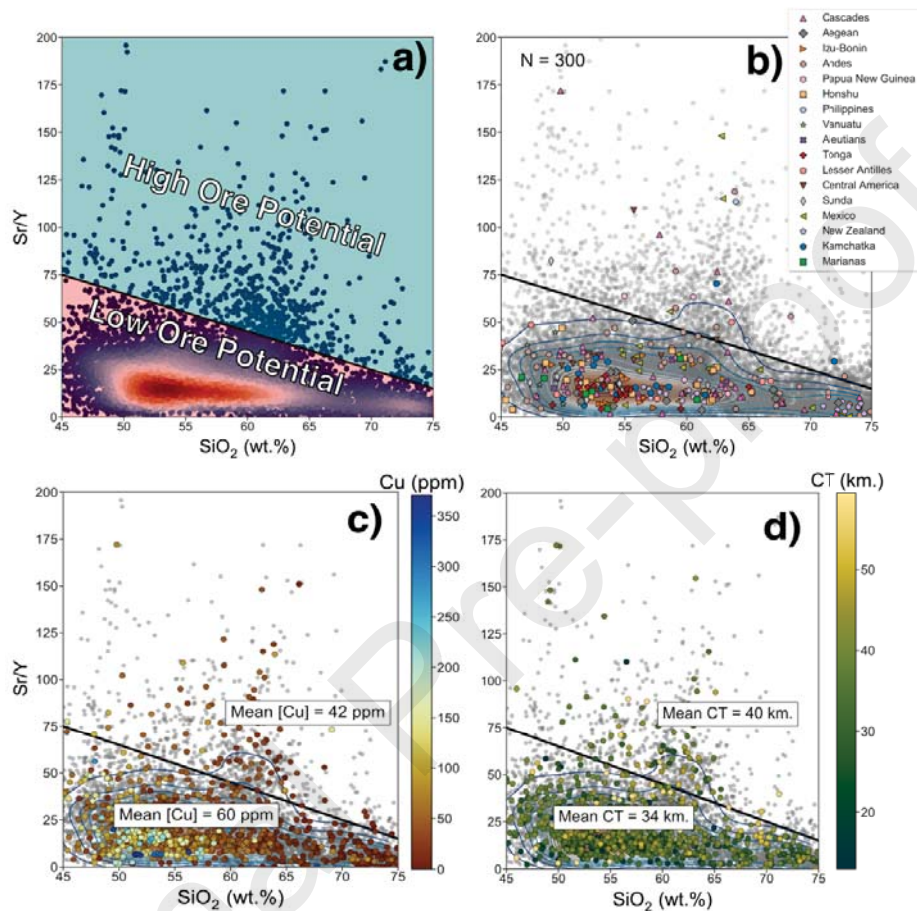
Figure 2: Sr/Y vs. SiO$_2$ plots, colored for different features. Plots b) and c) are both sub-sampled to only display 300 (b) and 1000 (c) samples for visual clarity. The black line called out in a) differentiates "high" from "low" ore potential, as defined in the literature [25]. Magmas sitting above the black line have higher ore formation potential. Plot a) is colored by the density of points in the total dataset, and contours for sample density are included in all subsequent plots. Plot b) shows a sub-sample of arc magmas colored and symbolized by arc; notice how ore-producing arcs are the only ones that tend to proliferate above the high ore potential line. Plot c) shows a sub-sample of the database colored for Cu, where high and low ore potential magmas have mean [Cu] of 42 and 60 respectively. Similarly, plot d) shows that high ore potential magmas have thicker crust, on average, than low ore potential magmas

47
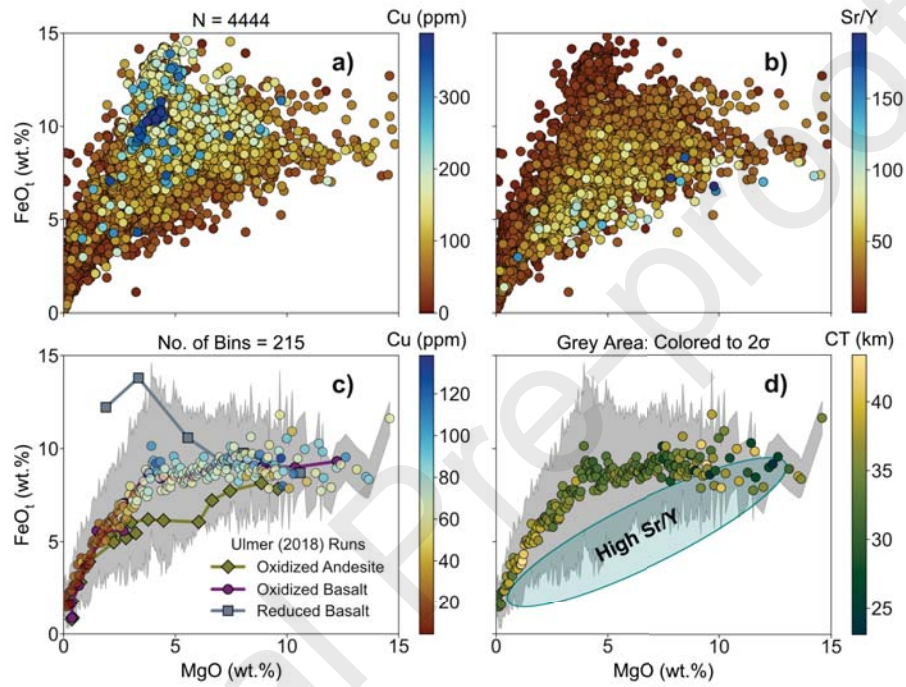
Figure 3: Differentiation trends for the entire dataset, colored for Cu in a) and Sr/Y in b). The highest Cu and Sr/Y measurements are ordered to plot on top of lower measurements. In (c) and (d), resampled averages are calculated for the full database (N = < 12,000) every 0.05 wt.% of MgO, colored for c) Cu (ppm) and d) Crust Thickness (km.). Errors colored out to 2σ, smoothed by a factor of 1.5 to reduce observed spread. Superimposed on the global database (c) are the empirical results of fractional crystallization experiments in arc conditions from [37]. Like Figure 5, blue ellipse is the area where high Sr/Y magmas plot in this Figure (5d)
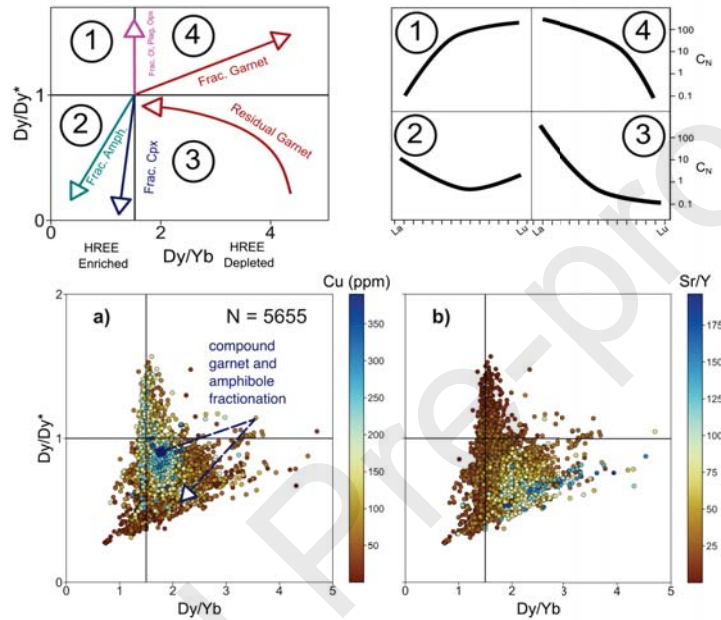
Figure 4: Panels showing the distribution of a) Cu and b) Sr/Y in Dy/Dy vs. Dy/Yb space. These Dy plots show relative fractionation trends according to which mineral phase is dominant. The starting point of each schematic mineral vector is in reference to a chrondrite normalized REE composition. The lowest Cu and highest Sr/Y magmas sit in an area generated by a combination of amphibole and garnet fractionation, and potential mantle source garnet melting. Points in a) and b) are ordered highest to lowest, with the highest Cu and Sr/Y stacked on top. Also shown as a blue ellipse is the area where high Sr/Y magmas plot in Dy/Dy* vs. Dy/Yb space. The dark blue arrow in plot a) shows the expected differentiation path of a magma ascending from high to low pressure, and experiencing first garnet, then amphibole fractionation. Such a liquid line of descent (LLD) can explain the spread in our high ore potential field.
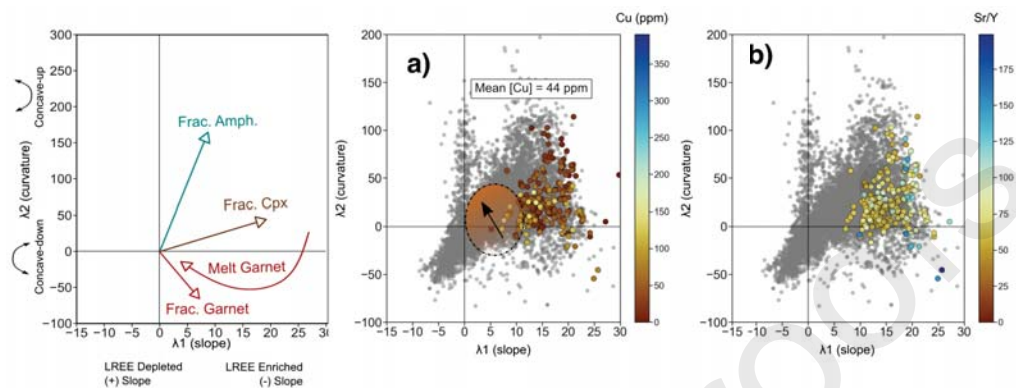
Figure 5: REE behaviour as described by λ spider-plot shape parameters [57]. Top panels are schematics, showing how $\lambda 1$ vs. $\lambda 2$ plots describe mineralogical controls on REEs during differentiation. While $\lambda 1$ describes slope, it is calculated according to the radius of ordered REEs. Hence, a negative $\lambda 1$ corresponds to a positively sloped REE spider profile. a) and b) plot $\lambda 1$ vs. $\lambda 2$ colored for Cu and Sr/Y respectively. Grey points show the entire global database. Colored points are those that plot in the high ore potential field of Figure 3. Mean [Cu] of high Sr/Y field given in a). Empirical results from [37] are shown in the orange shaded area in Figures a) and b), where the arrow denotes the evolving REE contents of empirical products in λ space.
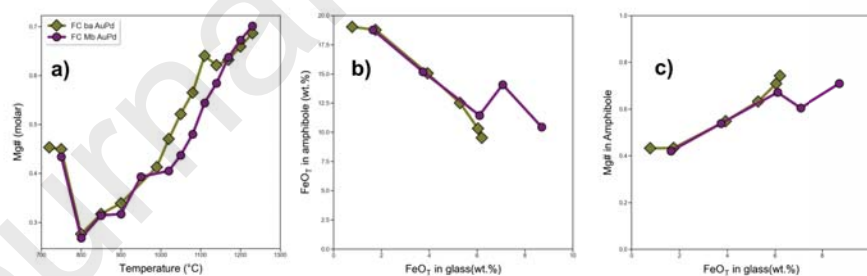

Figure 6: Compilation of melt compositions as compared to the crystallization time and chemistry of amphibole in the empirical products analyzed in this study[37]. Plot a) shows the melt Mg# as a function of temperature - amphibole stabilizes at 1050°C for both FC ba AuPd and FC Mb AuPd. Plot b) shows the FeO content of amphibole plotted against the FeO content of the corresponding silicate melt. Panel c) shows the amphiboles Mg# plotted against silicate melt FeO.
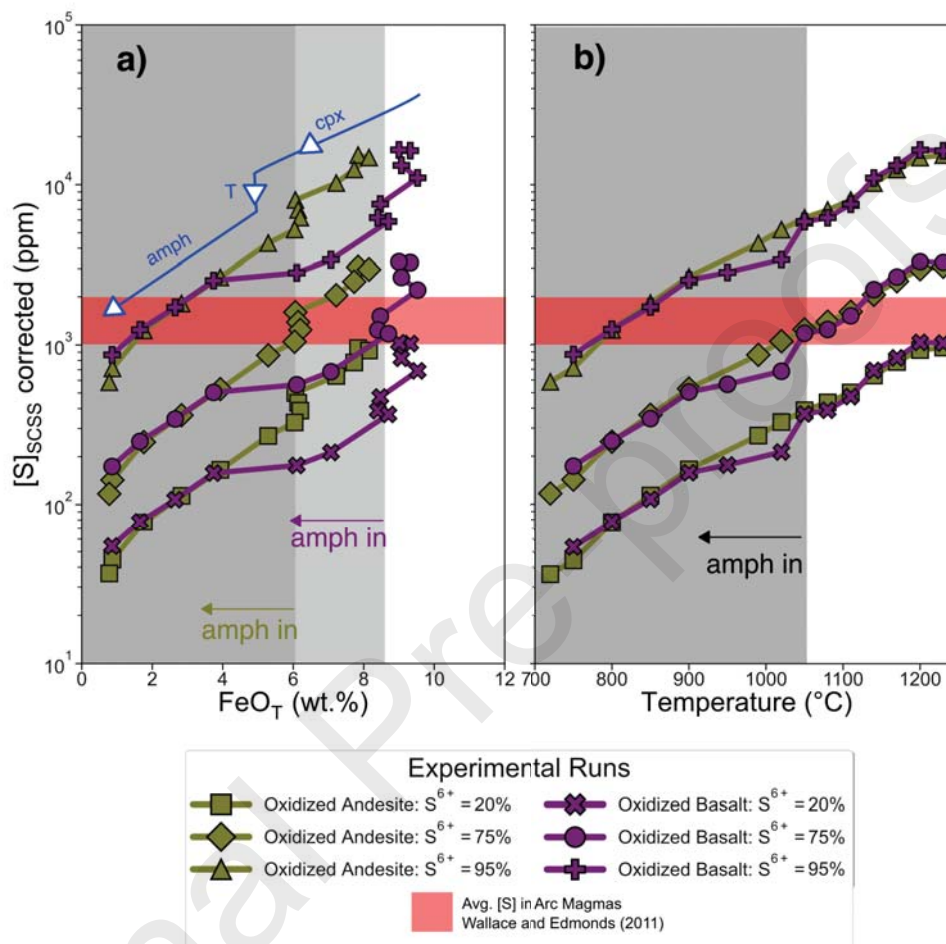
Figure 7: Empirical results of glasses from [37], using initial trace element abundances from [46, 67, 68], and the SCSS model of [29]. Plots show log(SCSS) vs. a) Total FeO and b) c) log(SCSS) vs. Temperature °C. Starting materials in each run were symbolized as: olive colored diamonds = oxidized andesite; purple circles = oxidized basalt;. Vertical grey bars indicate the onset of amphibole fractionation for the oxidized andesite vs. the oxidized basalt runs, respectively. Amphibole is measured to appear around 6.5 wt.% FeO and 1050 °C). SCSS of the model andesite was reported for 3 proportions of $S^{6+}/\Sigma S$ - 20%, 50%, and 90% respectively, following the corrections in [77]. The red box covering the area between 1000 and 2000 ppm [S] is the average minimum [S] content in arc magmas, taken from [75]. The thick blue line and associated blue labels show the inferred dominant-control on SCSS at different steps in the model. Discussion of partition coefficients used to model SCSS, Cu, and Sr/Y can be found in the main text and and Supporting Information)
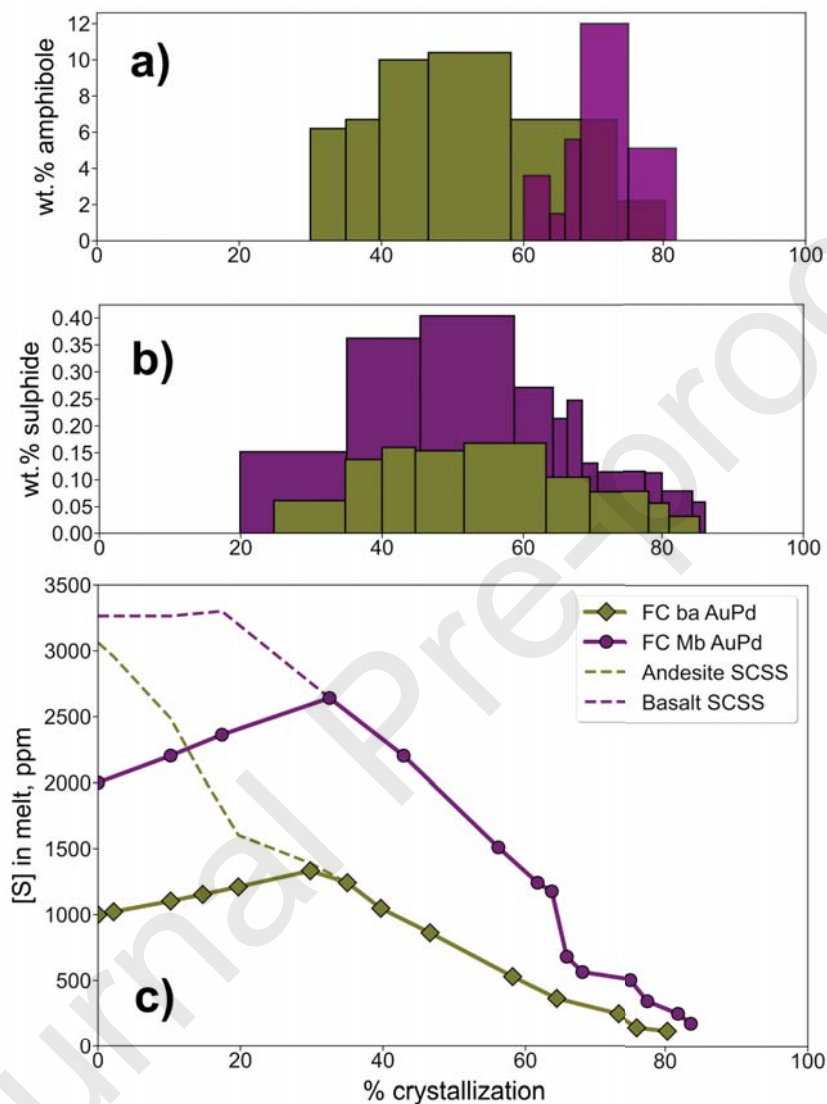
51

Figure 8: Mass balance of sulphur and sulphide in empirical datasets of oxidized calc-alkaline andesite (FC ba AuPd) and basalt (FC Mb AuPd)[37]. Panel a) shows the mass fractionation of amphibole crystallizing at each step in the experiments of Ulmer et al. 2018. The mass balance model for sulphur and sulphide, discussed in the text (Section 4.3.4) provides estimates of b) the mass of sulphide melt precipitating at each experimental step, and c) the trend in [S] in these kinds of melts. Initial [S] values were fixed at 2000 ppm for the basalt, and 1000 ppm for the andesite (see text for details). The precipitating sulphide had its composition adapted from average sulphide melts at Merapi volcano, Indonesia[22]
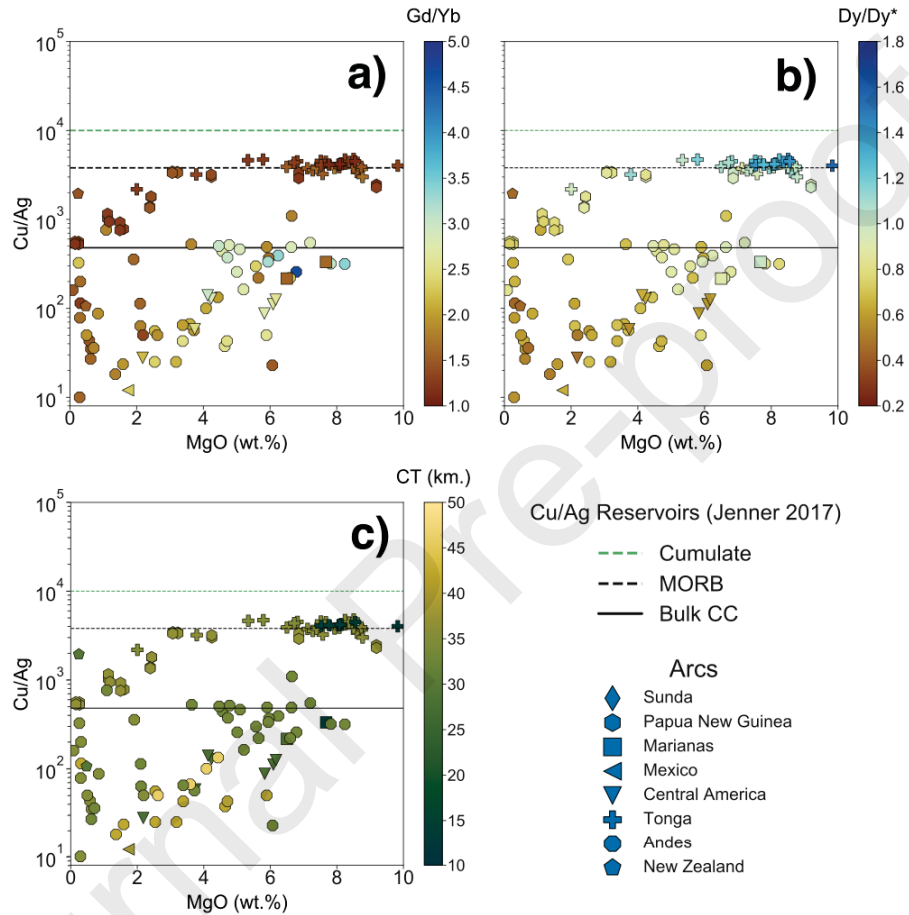
52

Figure 9: Cu/Ag (as a proxy for crystalline sulphide fractionation) plotted against MgO. Colored for a) Gd/Yb, b) Dy/Dy*, and c) Crust Thickness. Majority of samples plotted here are whole rock compositions. Individual samples are symbolized according to the arc they come from. Plot structure and reference lines for Cu/Ag adapted from [53], as are the reference compositions for Cu/Ag in Sulphide cumulates, MORB, and Bulk CC.
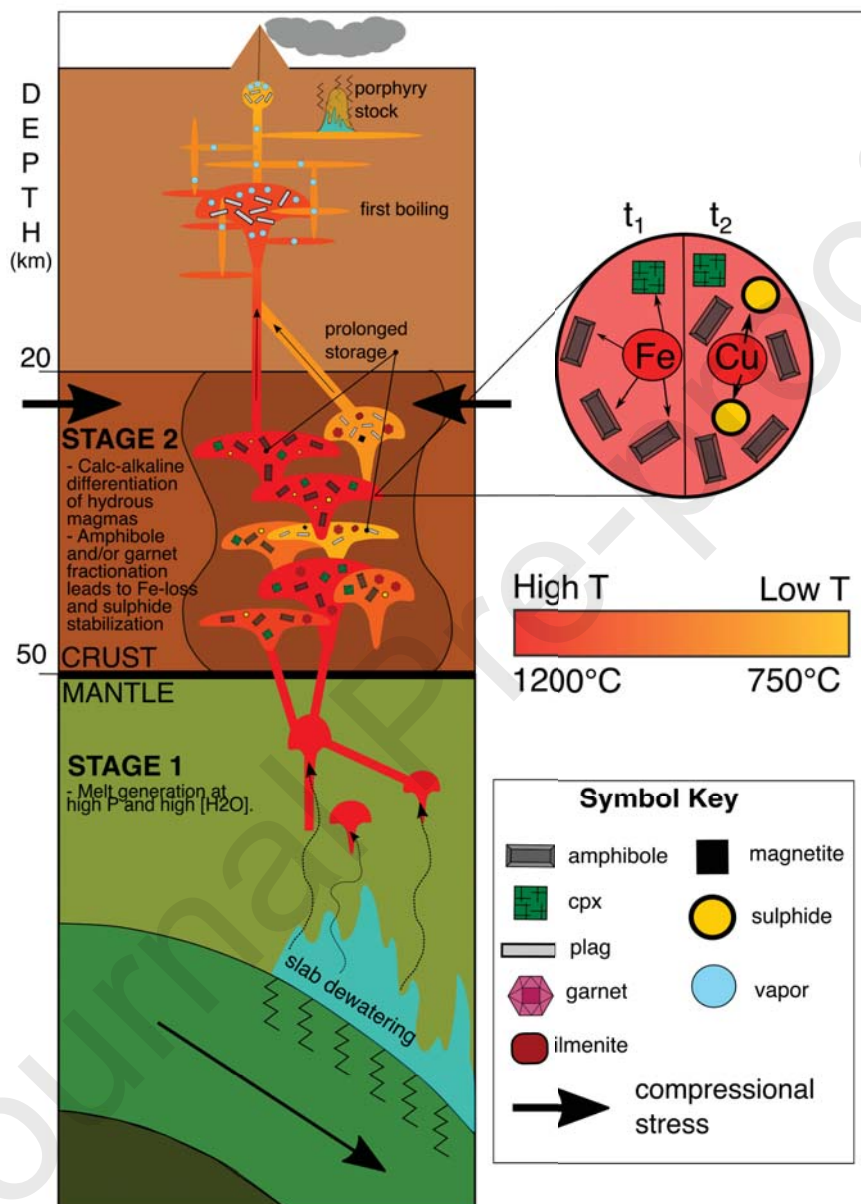
53

Figure 10: Our proposed model for Cu depletion in arc magmas. This model takes into account the different geochemical and geophysical signals picked out by our database. Stage 1 sees hydrous melting stabilize garnet in the mantle wedge under the right conditions, which imparts the Gd/Yb signal seen in some magmas in Figure 7. High water contents of these calc-alkaline primitive melts contribute to prolonged amphibole fractionation in Stage 2, where magmas staled at depth ($=/<$ 1 GPa) will fractionate enough amphibole to reduce [Fe] and stabilize sulphide. garnet fractionation likely plays a role at depths > 50 km, and could similarly deplete ore-fertile magmas in Fe, leading to sulphide fractionation.

Declaration of interests

☒ The authors declare that they have no known competing financial interests or personal relationships that could have appeared to influence the work reported in this paper.

☐The authors declare the following financial interests/personal relationships which may be considered as potential competing interests: